

# 5

## Simulations and synthetic observations using live stellar systems

*“The most exciting phrase to hear in science, the one that heralds new discoveries, is not ‘eureka!’ but ‘that’s funny’”*  
– Isaac Asimov, (1920-1992)

### 5.1 Introduction

In the previous two chapters we have shown the capability to create synthetic observations of the Galactic plane, specifically in CO emission. To do so we modelled the Milky Way as a grand design barred-spiral, whereby the arms and bars are fixed and have a constant pattern speed and morphology. While some of the features seen in observations could be reproduced, never were they all simultaneously. In this chapter we instead model the Milky Way stellar system as a set of discretised mass components, rather than a continuous density profile. Modelling a galaxy in this way is a tried and tested method and has been used to simulate both isolated stellar systems (Sellwood & Carlberg 1984; Sparke & Sellwood 1987; Sellwood & Sparke 1988; Shen et al. 2010; Grand et al. 2013; D’Onghia et al. 2013) and the simultaneous evolution of a gas disc (Carlberg & Freedman 1985; Elmegreen & Thomasson 1993; Clarke & Gittins 2006; Baba et al. 2009; Grand et al. 2012; Struck et al. 2011; Renaud et al. 2013; Athanassoula et al. 2013; Roca-Fàbrega et al. 2013). Simulations such as these, and many others, have shown that both bar and spiral features are surprisingly easy to reproduce, though not ones that necessarily agree with theory. For instance, spiral arms do not appear to be steady spiral density waves such as those suggested by Lin & Shu (1964), and bars are seemingly overabundant, and difficult to reproduce with accompanying spiral

structures.

In this chapter we first outline the computational method, and the procedure to generate the initial conditions of the simulations. We then show results various different simulations, and the accompanying gas morphology resulting from the evolution of the stellar system. The gas is then used to construct synthetic  $l$ - $v$  plots similarly to Chapter 4, where we utilise a similar tool to constrain the best fitting values for  $V_{\text{obs}}$ ,  $R_{\text{obs}}$  and  $l_{\text{obs}}$ . We briefly dedicate some time to quantifying the morphology of the best fitting simulations, e.g. the pitch angle and pattern speed of the arms, and compare these to the best-fitting maps of Chapters 3 and 4.

## 5.2 Modelling the stellar distribution with live particles in SPH

The computational method for evolving the ISM fluid is the same as that in Chapter 2. We utilise the SPH method with ISM chemistry and cooling to evolve the positions, velocities, energies and chemical abundances of the gas particles when exposed to the gravitational field of a Milky Way-like disc galaxy. While the method is essentially the same, some of the algorithms are slightly different (see Section 2.2.12). Instead of using a fixed potential with an analytic force field, we use numerous “star” particles in an  $N$ -body prescription. These star particles are not stars in the traditional sense. They emit no radiation, are all of uniform mass, and are constant in number throughout the evolution of the system. Most importantly, they are much more massive than any single star. Simulating the Galaxy on an individual star-by-star basis would be computationally crippling for the calculation of the gravitational force. Instead we use star particles whose mass is closer to that of a stellar cluster, with individual particles having masses of the order  $10^4$  to  $10^5$  solar masses depending on resolution and disc mass. These will be referred to simply as “stars” for the remainder of this chapter. Star particles behave similarly to SPH particles, but experience no hydrodynamical forces (i.e. are collisionless), and have no concept of internal energy. They therefore store no chemical information either. They do store a density, but this is used only for time-stepping, to ensure they are evolved in a similar manner to SPH particles. The main difference to the SPH particles is that they exert a gravitational force upon each other, and the individual gas particles. Details on the calculation of  $N$ -body forces, rather than those of a smooth potential, are given in Section 2.2. Gas particles still exert no gravitational forces upon each other, or the stars (i.e. no self-gravity in the gas), this is assumed to be negligible compared to the gravitation of the stellar system. In some instances we also use a live dark matter halo rather than fixed potential. As the general properties of the dark matter are still unknown, halo particles are simply more massive star particles.

### 5.2.1 Setting the stellar system

The initial conditions of particles in an  $N$ -body simulation are paramount to the evolution of the system, specifically the initial position and momentum vectors. In the previous chapters the initial gas distribution was relatively unimportant, with positions and velocities dominated by the effect of the external potentials shortly after their activation. However, in this instance the particles also provide the gravitational forces for the calculation, and so initial conditions can cascade into the

results seen much later in the simulation.

The method of setting initial conditions is adopted from Hernquist (1993), which is also used in Baba et al. (2009). The method requires density profiles of the separate Milky Way components; bulge, disc and halo. For the calculations here we always employ a live stellar disc. A bulge is also frequently used to match the Milky Way's rotation curve, though this has adverse effects on the efficiency of bar formation (see Sec. 1.3.4 and later in this chapter). Regarding the halo, we usually use a simple potential to represent the halo, due to its gravitational effect mostly dominating the outer disc, while the disc itself appears to primarily influence the gas dynamics. We do employ a live halo in some calculations, though the additional computational resources required to evolve a live halo require an overall reduction in resolution in the other mass components.

The density profiles we use are slightly different to those used in the previous chapter. Previously all that was needed of the potentials was for them to create a rotation curve that matched that observed, in effect reducing to a single force vector for each calculation. Here however the density distribution determines the stellar distribution, and in turn how it evolves over time. The density profiles chosen are therefore ones that have been tailored to match the Milky Way's mass/luminosity profile for each component. The bulge used is a spherical Plummer profile (Plummer 1911), with corresponding density, potential and velocity profile of

$$\rho_{\text{Plum}}(r) = \frac{3M_b r_b^2}{4\pi} \frac{1}{(r_b^2 + r^2)^{5/2}} \quad (5.1)$$

$$\Phi_{\text{Plum}}(r) = -\frac{GM_b}{\sqrt{r_b^2 + r^2}} \quad (5.2)$$

$$V_{\text{Plum}}^2(r) = +r \frac{GM_b}{(r_b^2 + r^2)^{3/2}} \quad (5.3)$$

where  $M_b$  and  $r_b$  define the characteristic mass and scale length. Initial calculations were made using a Hernquist profile bulge but due to the relatively stronger concentration at small radii, problems were encountered when setting the initial smoothing lengths of the particles. A spherical bulge is a slight simplification, as in the Milky Way the inner bar is often indiscernible from the bulge. However, we make no assumption about a bar morphology, and instead allow bars to naturally occur in the disc evolution. The stellar disc, containing the majority of stellar material, follows an exponential density profile (Binney & Tremaine 1987) so called due to the surface density profile of the form

$$\Sigma_{\text{Exp}}(r) = \frac{M_d}{2\pi R_d^2} \exp(-r/r_d) \quad (5.4)$$

which can be generalised to a volume density with the inclusion of a  $\text{sech}^2(z)$  vertical scaling

$$\rho_{\text{Exp}}(r, z) = \frac{M_d}{4\pi R_d^2 z_d} \exp(-r/r_d) \text{sech}^2(z/z_d) \quad (5.5)$$

where characteristic masses and scale lengths are  $M_d$ ,  $r_d$  and  $z_d$ . Integrating  $\rho_{\text{Exp}}$  over  $z$  reduces

vertical dependance to  $2z_d$  and returns the disc surface density. The 2D potential and velocity profile are

$$\Phi_{\text{Exp}}(r) = -\frac{GM_d r}{2r_d^2} \left[ I_0\left(\frac{r}{2r_d}\right) K_1\left(\frac{r}{2r_d}\right) - I_1\left(\frac{r}{2r_d}\right) K_0\left(\frac{r}{2r_d}\right) \right] \quad (5.6)$$

and

$$V_{\text{Exp}}^2(r) = \frac{GM_d r^2}{2r_d^3} \left[ I_0\left(\frac{r}{2r_d}\right) K_0\left(\frac{r}{2r_d}\right) - I_1\left(\frac{r}{2r_d}\right) K_1\left(\frac{r}{2r_d}\right) \right] \quad (5.7)$$

where  $I_0, I_1$  and  $K_0, K_1$  are modified Bessel functions of the first and second kind respectively. A NFW dark matter halo is adopted (Navarro et al. 1996) which takes the form

$$\rho_{\text{NFW}}(r) = \frac{\rho_0}{r/r_h(1+r/r_h)^2} \quad (5.8)$$

where

$$\rho_{\text{NFW},0} = \frac{M_h}{4\pi r_{200}^3} \frac{C_{\text{NFW}}^3}{\ln(1+C_{\text{NFW}}) + C_{\text{NFW}}/(1+C_{\text{NFW}})}. \quad (5.9)$$

and  $M_h$ ,  $r_h$ ,  $r_{200}$  and  $C_{\text{NFW}}$  are constants to be set.  $r_{200}$  defines the halo viral radius, and  $r_h$  is related by  $r_h = r_{200}/C_{\text{NFW}}$ . The resulting potential and velocity profiles are

$$\Phi_{\text{NFW}}(r) = -4\pi G \rho_{h,0} r_h^2 \frac{\ln(1+r/r_h)}{r/r_h}, \quad (5.10)$$

and

$$V_{\text{NFW}}^2(r) = -GM_h \left( \frac{1}{r_h} (1+r/r_h)^{-1} - \frac{1}{r} \ln \left[ 1 + \frac{r}{r_h} \right] \right) \frac{1}{\ln(1+C_{\text{NFW}}) - C_{\text{NFW}}/(1+C_{\text{NFW}})}. \quad (5.11)$$

In the case of a fixed halo, this is all that is needed to calculate the forces for the gas and star particles.

The density profiles for each component are used to set the positions of the star particles. The density profile effectively represents the number density of the star particles of that mass component, providing the masses are all the same. The density can thus be used as the probability distribution function (PDF) for the stars. Once correctly normalised, this can then be integrated to obtain the cumulative distribution function (CDF) in the range of 0-1. By drawing random numbers and finding the equivalent positions from equating to the CDF, the particles can be placed “randomly” in accordance with a predefined density profile. Figure 5.2 shows an example of this for the exponential disc. In the left panel is the surface density profile (red line), PDF (magenta line) and CDF (blue line). The histogram and black points correspond to the star particles position and corresponding surface density drawn from these distributions, showing good agreement with the input functions. On the right is the resulting  $x$ - $y$  positions of the 10000 particles, once allocated a random azimuthal position is drawn from a uniform distribution.

Minor complications arise when using the density profiles above. None of the profiles are constrained to a finite volume, and so require either the radial extent to be artificially limited (but this can lead to artificial truncation of the mass distribution) or to add a ad-hoc truncation profile over some distance  $r_t$ , e.g. with an additional  $\exp[-(r/r_t)^2]$  term in the density profile.

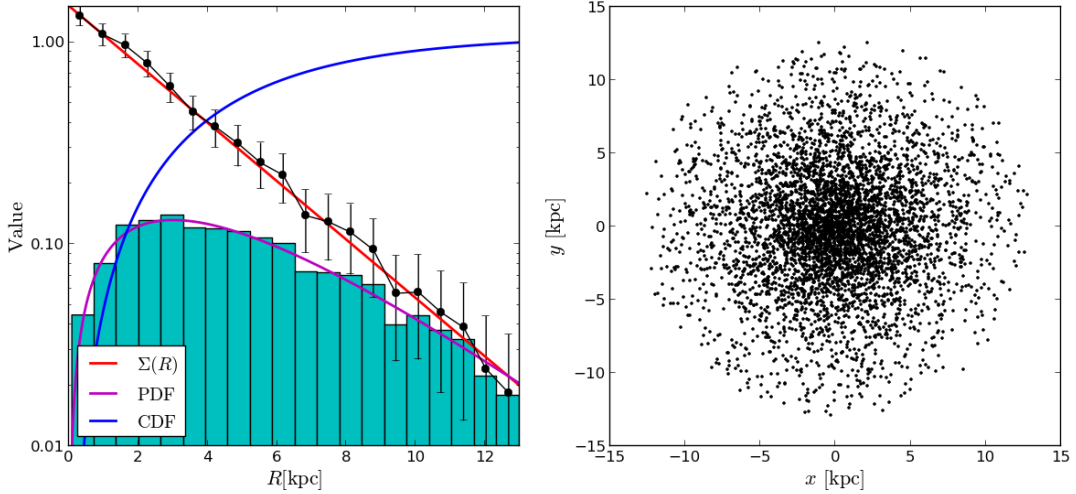


Figure 5.1: Example of setting the initial positions of particles. On the left is the surface density profile (red), resulting PDF (magenta) and CDF (blue) as a function of radius for the exponential disc. The resulting particle positions chosen from these functions is shown to match the PDF, and the underlying surface density (black points, with errors scaling as the size of histogram bins). The resulting  $x$ - $y$  positions of the particles is shown in the right panel.

The truncation distance is chosen carefully as to ensure the total mass of the component is not significantly altered (e.g.  $r_t = 4\text{kpc}$  for the bulge). This makes calculation of the CDF for the halo sufficiently complicated that a Taylor expansion to the eighth term was used for the integration.

Drawing the velocities is significantly more complicated, but primarily requires integrating the separate moments of the collisionless Boltzmann equation, a.k.a Jean's equations (i.e. differential equations in velocity components in the  $R$ ,  $z$  and  $\theta$  directions with respect to  $R$ ). This procedure can give mean velocity components, which can then be used with some sensible source function, such as a Gaussian, to draw actual velocities for each particle (see Hernquist 1993 for details). This process requires density, potential, velocity and mass profile functions for each component, and requires numerical integrations of combinations of Equations 5.1 to 5.11, requiring numerical integration schemes. Velocities of the disc are circular with some dispersion, while the velocities of the halo and bulge are in random orientations. Tests were made where the bulge had a non-zero streaming fraction, i.e. fraction of orbits aligned with net disc rotation, but this had minimal impact on the disc evolution. The initial value of the Toomre  $Q$  parameter must be defined for the disc to calculate the velocity dispersion. We use a value of  $Q_s = 1$  to ensure the disc is borderline stable to arm formation. We experimented with other initial values of  $Q_s$ , and found 1 to be a good value for seeding spiral structure while keeping the disc from experiencing dramatic radial density waves and avoiding an over-clumpy stellar distribution. Occasionally velocities are generated nearing the escape velocity of the system, if this is the case a new velocity is drawn (Hernquist 1993).

We use the SPH code `SPHNG` for the work presented in this chapter, which is described in Section 2.2.12. As with any  $N$ -body code, it is prudent to soften the gravitational force to avoid

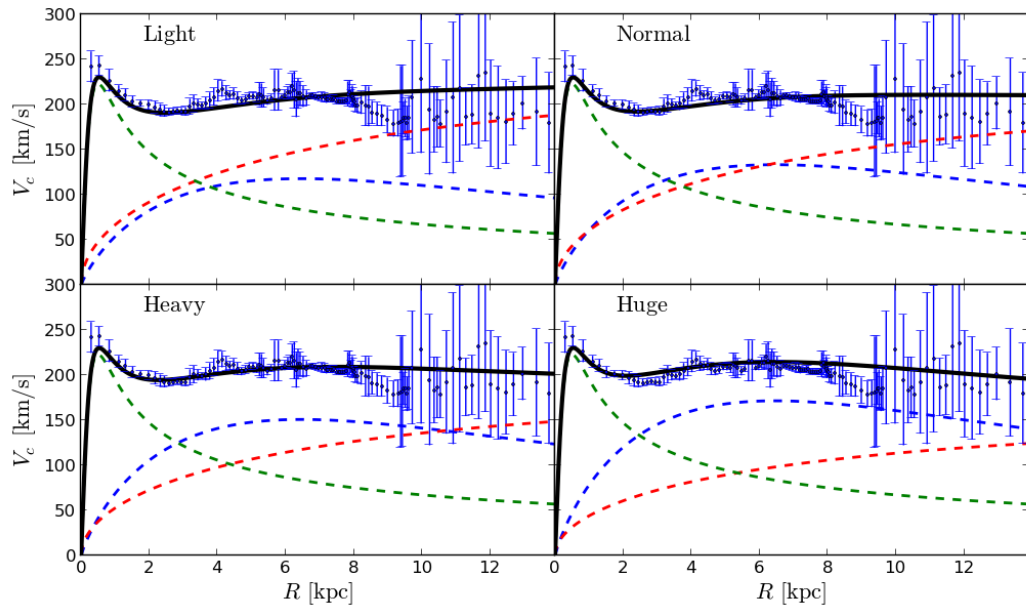


Figure 5.2: Axisymmetric rotation curves for calculations presented in this chapter. Disc, bulge and halo components are shown as the red, green and blue dashed lines respectively. Four different models are shown with labels referring to the disc mass; “light”, “normal”, “heavy” and “huge”. The halo mass is adjusted in each case to ensure a rotation curve that is in agreement with observations (blue points, from Sofue 2012).

problems during close encounters between particles. SPHNG incorporates adaptive softening lengths for the gas and star particles. The gas particles simply use the hydrodynamical smoothing length scale. The stars use a value that is calculated from nearest neighbouring star particles, identical to the method of calculating the smoothing lengths of SPH gas particles. The difference being the smoothing length of  $N$ -body particles is not used for a hydrodynamical force. The implementation of which is described in detail in Price & Monaghan (2007). Approximate softening values for gas and star particles are 20pc and 100pc respectively, but differ greatly depending on environment.

Due to the nature of an  $N$ -body methodology imbedded in an SPH structured code, there are occasionally difficulties when setting the initial smoothing lengths of the star particles due to the large difference of masses between the gas and star particles. To overcome these problems we occasionally seed a stellar system with a resolution 1/9 lower than that desired. This relatively small number of particles,  $O(10^5)$ , without a gas disc is easily set by the code. This is then allowed to evolve for a very small timestep. After which the resolution is increased by simply transforming the point particle into a body-centred cubic lattice with vertices 0.6 times the smoothing length of the parent particle, and mass split between them accordingly. As setting up cubic lattices can induce spurious structure, we rotate each lattice randomly in each direction after splitting. The resulting system evolves very similarly to the original, low-resolution one. A gas disc is then imposed on the stellar distribution.

In the calculations in the previous chapter, how the mass in stars was distributed between the bulge-disc-halo system was irrelevant so long as the resulting rotation curve agreed with ob-

Term	Description	Value
$M_d$	Disc mass	$2.5, 3.2, 4.1, 5.3 \times 10^{10} M_\odot$
$M_h$	Halo mass	$10.1, 8.3, 6.3, 4.4 \times 10^{11} M_\odot$
$M_b$	Bulge mass	$1.05 \times 10^{10} M_\odot$
$r_d$	Disc radial scale length	3.0 kpc
$z_d$	Disc vertical scale length	0.3 kpc
$r_{200}$	Halo radial scale length	122 kpc
$C_{NFW}$	Halo concentration factor	5
$r_b$	Bulge radial scale length	0.35 kpc

Table 5.1: Fixed galactic axisymmetric potential parameters used to reproduce the observed rotation curve in calculations with a live stellar component. The four values for  $M_d$  and  $M_h$  indicate our four configurations for the different disc to halo mass ratios. The resulting rotation curves are shown in Figure 5.2.

servations. Here this is not the case as the mass in the disc is directly delivered to the disc and bulge star particles. As there is some uncertainty regarding the mass of the Milky Way components we use four separate bulge-disc-halo configurations, the rotation curves for each are shown in Figure 5.2 with the respective parameters for the “light”, “normal”, “heavy” and “huge” configurations (ordered by increasing disc mass) given in Table 5.1. We keep the bulge initial conditions the same for all calculations and use different disc and halo masses to reproduce the observed rotation curve. The values for the “normal” setup are based on those from Baba et al. (2009). The bulge mass is unchanged, with the disc to halo mass ratio being the effective variable. The different disc masses also allow for greatly different swing amplified spiral modes (Equation 1.9 and Dobbs & Baba 2014) ranging from  $2 \leq m \leq 5$ . Thus while we do not have direct control over the spiral structures formed in these calculations, we attempt to drive a range of spiral modes induced by swing amplification.

A final point to note is the setting of gas particles. We set gas on similar orbits and positions to the star particles, only with much lower masses in accordance with a gas disc of the same mass as the previous chapters ( $8 \times 10^9 M_\odot$ ) for consistency. Gas was not distributed according to the observed surface density profile however, but rather in an exponential disc. As the stellar disc is live, there is room for the surface density to settle itself due to the complex motions of the stellar system. We wanted to allow for the stellar distribution to drive the gas around the disc, rather than assume some profile. The resulting resolutions adopted for each set of computations is approximately 1 million disc star particles, and 0.1 million bulge particles. For simulations with a live halo 0.95 million disc, 50000 bulge and 0.5 million halo particles are used. In our high resolution calculations, 3 million gas particles are used. While 5 million was seen to be optimal in the previous chapters, we performed tests with 1 million and find the emission features are less sensitive to resolution. One million did however make weaker arm features in the edge of the disc, where particle density becomes low. We use 1 million gas particles for lower resolution tests, some of which are shown in this chapter.

We also allow for the creation of sink particles in these calculations (Bate et al. 1995). In simulations with  $N$ -body gravitational forces it is possible that the density of the gas in certain regions becomes extremely high as the gas accumulates around some point, such as a small cluster

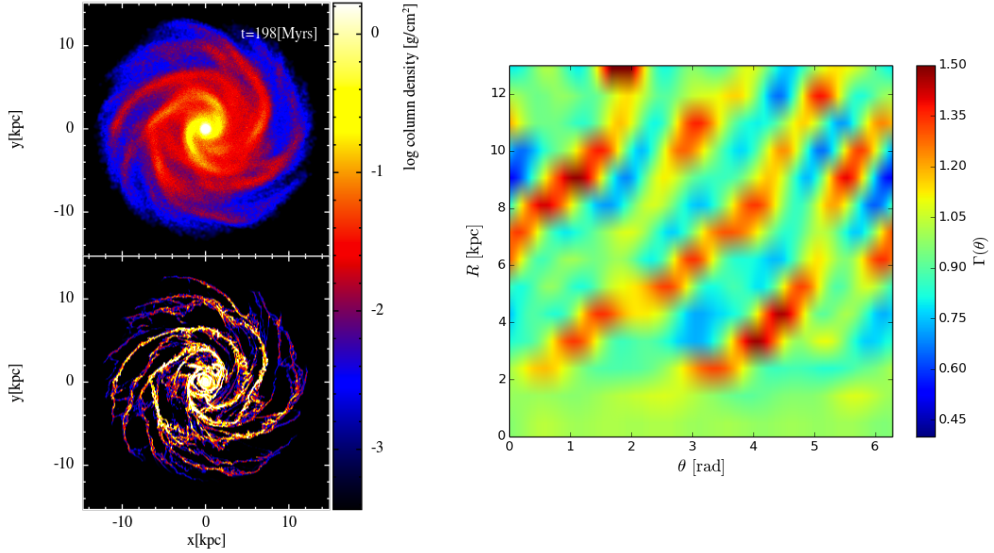


Figure 5.3: Projection of material in a simulation with a live disc and bulge into  $R - \theta$  space. In the left panel the density of the stars (top) and gas (bottom) is shown. In the right panel the stellar material has been binned and normalised by surface density.

of star particles. To allow the computation to proceed further the gas clump is replaced by an accreting point-mass particle; a sink. These sinks act via gravitation with the remaining particles, and are allowed to accrete additional gas as they traverse the disc. Very few sinks are formed in these simulations (one or two, if any) and they have minimal impact on the global gas morphology.

### 5.3 Measuring arm number, pitch angle and pattern speed

One of the main differences between the models with a live stellar component and those with fixed analytic potentials in previous chapters is that we do not know the arm number, pitch angle, and pattern speed of features formed. While we can at least estimate a dominant arm mode from swing amplification (Equation 1.9), other values are complete unknowns until the calculation is performed. We use numerous methods to quantify these values from our calculations, so they can be compared to observational determined values, and those of the previous chapters. The methods outlined here are similar to those used in previous studies (Dobbs et al. 2010; Fujii et al. 2011; Grand et al. 2012; D’Onghia et al. 2013), e.g. using Fourier transforms to find arm number, and will be illustrated by an example simulation. An important caveat to this and the rest of the methods below is that the arm shape is assumed logarithmic and periodic, i.e. with each arm separated by  $2\pi/N$ .

#### Arm number

The simplest way to measure arm numbers numerically is to take a Fourier transform of the Galactic material. The data is first projected into  $R - \theta$  space, where logarithmic spiral arms will appear as diagonal lines. The data is binned into an  $R - \theta$  grid, which is then normalised by the surface

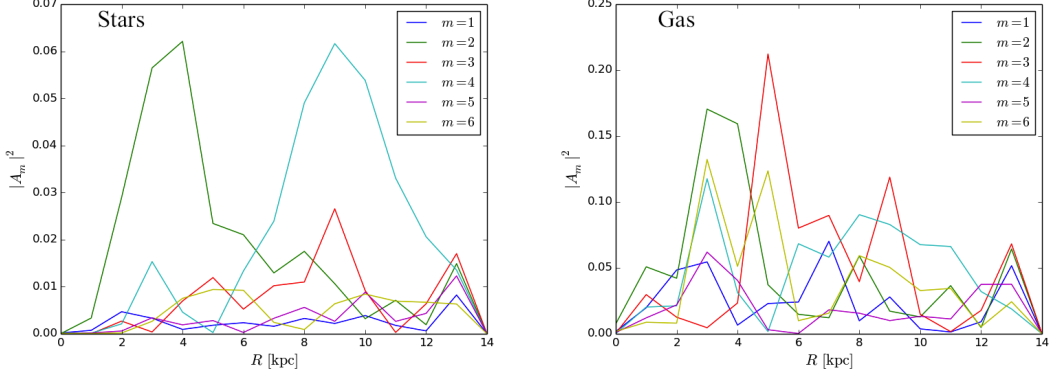


Figure 5.4: Amplitude of Fourier modes as a function of radius in stellar (left) and gaseous (right) material in the calculation shown in Figure 5.3. Different modes are shown as different coloured lines. Note the stellar material has much clearer structure than that of the gas.

density of the disc to ensure that inner arm structures do not dominate the fit. This gives the surface density contrast at a given radius:  $\Gamma|_R(\theta) = \Sigma(R, \theta)/\Sigma(R)$ . In Figure 5.3 we give an illustration. In the left panel is the top-down column density of the stars (top) and gas (bottom) in a simple live disc-bulge model. In the right panel is the corresponding normalised surface density of the stars in  $R - \theta$  space. Notice the over-densities appearing in diagonal lines, tracing out the spiral arms. The stellar distribution tends to be much smoother than the gaseous distribution, making fitting to arm number and pitch less susceptible to being driven by small armlets or inter-arm features.

A Fourier transform is then performed on  $\Gamma|_R(\theta)$  at different radii (this is done every kpc). We use the FFT module of the NUMPY PYTHON package. We then extract the dominant mode at that given radius (i.e.  $\Gamma|_R(\theta)$  array) in the range  $1 \leq m \leq 6$ , which is then dubbed the dominant spiral mode for that calculation in that time-frame. An example of Fourier modes for the calculation in Figure 5.3 is shown in Figure 5.4. The dominant modes for the stellar and gaseous components are shown in the left and right panels respectively. For the stars it appears a 2-armed structure dominates the inner disc, which then transforms into 4-armed pattern in the outer disc (beyond the Solar position). This can also be seen by-eye in Figure 5.3, where there are two clear inner arms in the stars and a weaker, yet noticeable, 4-armed pattern further out. Again, the dominant modes are much clearer in the stars as opposed to the gas. While both show a  $m = 2$  dominant mode in the inner disc, the gas has a strong  $m = 3$  mode in the mid disc.

The strongest Fourier mode is taken to be the arm number, though in some instances, such as Fig. 5.4, there are two conflicting modes due to the variation as a function of radius. The location of the dominant modes that are shown in Figure 5.4 are shown in Figure 5.5 (stars only), with each panel corresponding to a different value of  $m$ . This figure confirms what is shown in Figure 5.4, that the  $m = 4$  mode dominates the outer disc, and the  $m = 2$  mode dominates the inner disc.

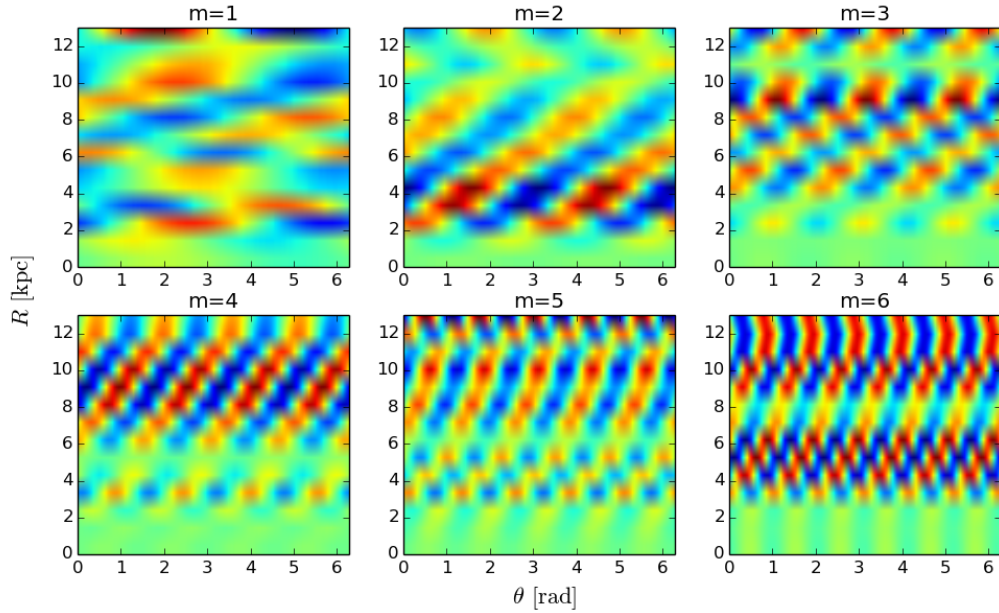


Figure 5.5: Location in  $R - \theta$  space of the dominant modes in Fig. 5.4, shown for the stars only. If all modes are combined together they will approximately return the map in the left of Figure 5.3 (neglecting  $m > 6$  terms).

### Pitch angle

Once a dominant arm number is known (or selected) the pitch angle can be calculated. We can choose to fit to any spiral mode, i.e. any panel of Figure 5.5. This is useful for calculations where arm features are compared across multiple time-frames such as the calculation of the pattern speed, where the arm number is assumed to be time-independent. We first extract the  $R - \theta$  position of the required mode. Depending on the morphology, this may only be done across a certain radial extent, such as the range in which that mode dominates (e.g. from  $2\text{kpc} \leq R \leq 6\text{kpc}$  for the  $m = 2$  mode in Fig. 5.5). The pitch angle,  $\alpha$ , of a logarithmic spiral arm is linked to the values of the constant  $B$  in the equation

$$\theta = f(R, \alpha) = B(\alpha) \ln R + C \quad (5.12)$$

where the pitch angle is  $\alpha = \arctan B$  and  $C$  defines the azimuthal position of the arms. This equation is then fit to the relevant mode, and uncertainties are added at each radius ( $\sigma_\Gamma$ ), proportional to the inverse of the value of  $\Gamma|_R(\theta)$  thereby adding weight to the regions of greater density. The fitting is done using a downhill Nelder-Mead simplex algorithm from the SCIPY PYTHON package and minimising a chi-squared like statistic of the form

$$\chi = \frac{1}{n} \sqrt{\frac{\sum_i (f(R_i, \alpha) - \theta_i)^2}{\sigma_\Gamma^2}} \quad (5.13)$$

over all  $i$  points in the arm ( $n$  total). To perform such a fit an initial guess is needed for the  $B$  and  $C$  parameters. Usually the fit is unaffected by these values, but we test numerous values to check

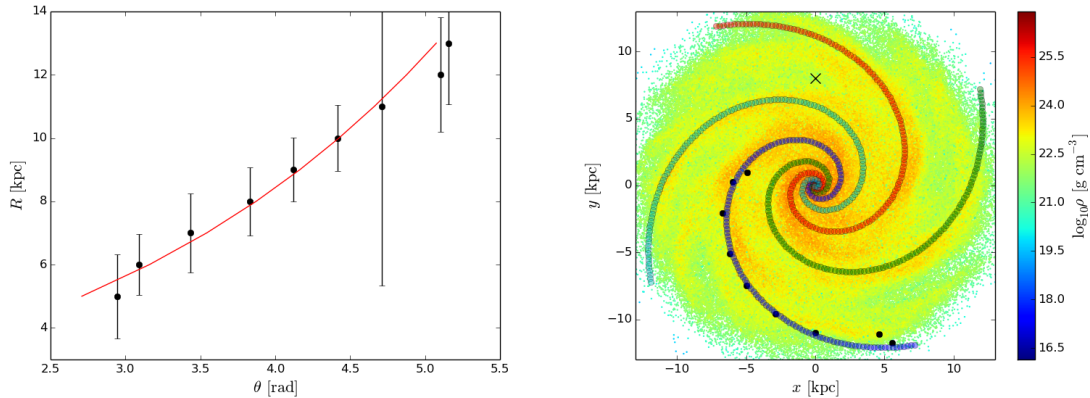


Figure 5.6: Fitting the pitch angle of an arm to a stellar disc. In the left panel are points used in the fit, shown in black, and the corresponding best-fit arm model shown as the red line ( $\alpha \approx 20^\circ$ ). In the right panel is the  $m = 4$  model over-plotted onto the stellar disc, where particles are coloured by density.

for consistency (confirming any spurious fits by-eye).

An example of the fit to the  $m = 4$  stellar mode in Figure 5.5 is shown in Figure 5.6. The left panel shows the points that trace out the arm (black points) and the best fitting logarithmic spiral arm (red line). In the right panel the top down position of the disc star particles is shown, coloured by particle density, with the same points as in the left panel over-plotted along with the best fitting  $m = 4$  arm model. In this instance the best fitting model has a pitch angle of approximately  $\alpha = 20^\circ$ . This can change up to  $\pm 2^\circ$  depending on the radial extent of the disc used in the fit.

### Pattern speed

While there exists some complex methods of determining the pattern speed from an observers perspective (e.g. Tremaine & Weinberg 1984) we choose to simply calculate the azimuthal offset between arm features over a given time frame. This approach is often adopted in numerical works, as we are in the privileged position of knowing the morphology at different epochs (Dobbs 2011b; Grand et al. 2013).

For any given calculation we first calculate arm number and fit a pitch angle. We then take subsequent time-steps and perform the same fit to arms, only this time fixing the arm mode to fit to. Then by simply calculating the offset between arms at different epochs the pattern speed can be calculated as a function of radius. In Figure 5.7 we show such a calculation. In the left panel are the traces of the best-fitting  $m = 4$  mode for the simulation shown in Figure 5.3 (again, stars only) and at four later time-steps spanning  $\approx 40$  Myrs. The resulting pattern speeds are shown in the right panel by the coloured points, where the speed has been calculated using adjacent time-frames only. The dashed line shows the pattern speed calculated using all time-frames (i.e. using the first and last frame). In all instances a clear decrease of pattern speed with radius can be seen, indicating the arms act as material, rather than wave-like features. The average pattern speed across all time-frames and radii in Fig. 5.7 gives a value of  $\Omega_p = 24 \text{ km s}^{-1} \text{ kpc}^{-1}$ .

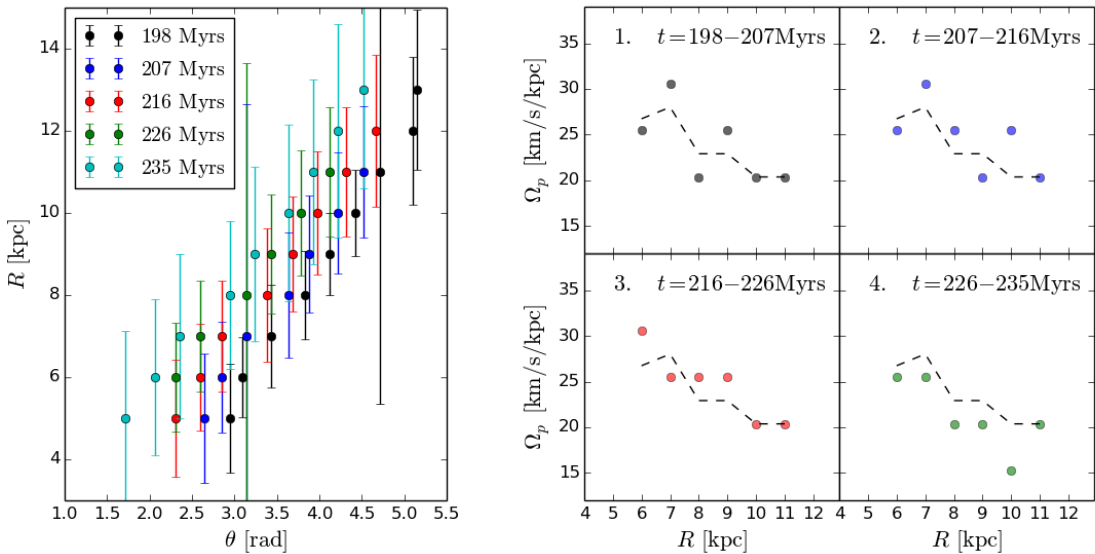


Figure 5.7: Illustration of fitting to the pattern speed in a calculation with a live stellar component. In the left panel is the tracing of best-fitting arm structures for the  $m = 4$  mode across 40 Myr of evolution of the calculation shown in Figure 5.3. The offset of each arm to the neighbouring time-frame is used to calculate a pattern speed for the spiral arms as a function of  $R$ , shown in the right panel by the coloured points. The dashed line is the pattern speed across all five time-frames.

The arm structure is assumed to be constant with time using this method. This is not entirely the case, seen by the fact that best-fitting pitch angles change between time-frames in Figure 5.7, with values ranging from  $22^\circ \leq \alpha \leq 19^\circ$ . However, the dominant arm modes appear constant over this time, i.e. the general trends in Figure 5.4 remain largely unchanged (in the stars).

## 5.4 Results of simulations

In this section we describe the results of our simulations using a live stellar distribution for the disc, bulge and, in some instances, halo. Discussion of the  $l$ - $v$  maps will be done in Sections 5.5 and 5.6.

The full set of simulations is given in Table 5.2. The “heavy” configuration is more of our default rather than the “normal” (so named as it matches the values of Baba et al. 2009). The “normal” setup tended to create a many armed structure ( $4 < m < 5$ ) in test simulations, so we made our default a disc with a slightly higher mass to drive a slightly lower arm mode. We run live disc only (D), live disc and bulge (B) and live disc, bulge and halo (H) calculations in a range of mass configurations; a,b,c and d (see Table 5.1 and Figure 5.2). The D and B calculations use a fixed analytic halo potential but we also perform two calculations using a live halo and the “heavy” mass disc, Hb. A few special case calculations were also performed. The first case is to evolve the stellar system of each type of model for 1Gyr before the addition of gas (DbG, BbG and HbG models). The aim was to see what kind of structure can be created in a settled disc.

Calculation	Description
Db	Live disc <i>only</i> in “heavy” configuration
Dc	Live disc <i>only</i> in “normal” configuration
DbG	As Db but allowing for 1Gyr of evolution before addition of gas
Ba	Live disc and bulge in “huge” configuration
Bb	Live disc and bulge in “heavy” configuration
Bc	Live disc and bulge in “normal” configuration
Bd	Live disc and bulge in “light” configuration
BbL	As Bb but with half gas disc mass
BbG	As Bb but allowing for 1Gyr of evolution before addition of gas
Hb	Live bulge, disc and halo in “heavy” configuration
HbG	As Hb but allowing for 1Gyr of evolution before addition of gas

Table 5.2: Description of different live-disc models. Refer to Table 5.1 and Figure 5.2 for the disc and halo mass ratio configurations. If halo is not listed as live then it is represented by an analytic potential. All models contain the same configuration of gas disc except BbL. All apart from DbG and HbG contain 3 million gas particles models.

Previous *N*-body work has shown that without some method dissipation, either by addition of gas or accretion, spiral arms will slowly dissipate (Sellwood & Carlberg 1984). To this end, we aimed to see if a generally featureless disc could reproduce *l-v* features of our Galaxy. One final calculation is our fiducial setup (Bb in Table 5.2) with half the normal gas disc mass ( $4 \times 10^9 M_\odot$ ) to see whether a reduced disc mass will reproduce sufficient CO emission in a live disc; BbL. It produced significantly weaker emission when using fixed potentials (Figure 4.3).

### 5.4.1 Live disc only

The simplest calculation performed was to calculate the evolution of a stellar disc, without the presence of a bulge but with an analytic halo to maintain outer velocity structure. The evolution of such a system (with a disc mass/halo mass of the “normal” configuration) is shown in Figure 5.8. The stellar distribution is shown in the top panels and the gas in the bottom, where all material is rotating clockwise. Arm structures can clearly be seen in the stars and gas. The nature of these arms is discussed in more detail in Section 5.4.2. These arms host a majority of the molecular gas in the simulation. As gas leaves the arm it experiences a drop in density and has a rapid decrease in molecular content, until the eventual passage into another spiral arm. Similar to the previous calculations, the vertical structure in the gas collapses into the plane rapidly, though the somewhat more turbulent nature of the stellar potential makes the disc thickness greater than when using an analytic potential. We maintain that stellar feedback may be required to substantially drive gas away from the plane.

Figure 5.8 shows a mild shockwave of material emanating from the centre at early times (also visible in the rotation curve). This is seen in other *N*-body calculations, and can be reduced by allowing for the disc to evolve for some time and periodically re-setting azimuthal positions to avoid arm growth (Fujii et al. 2011). We find these structures are resolution dependant, and in lower resolution cases the effect is much clearer. Originally we ran a “Huge” disc configuration (a would be Da model) but found these radially propagating rings having too strong an effect on

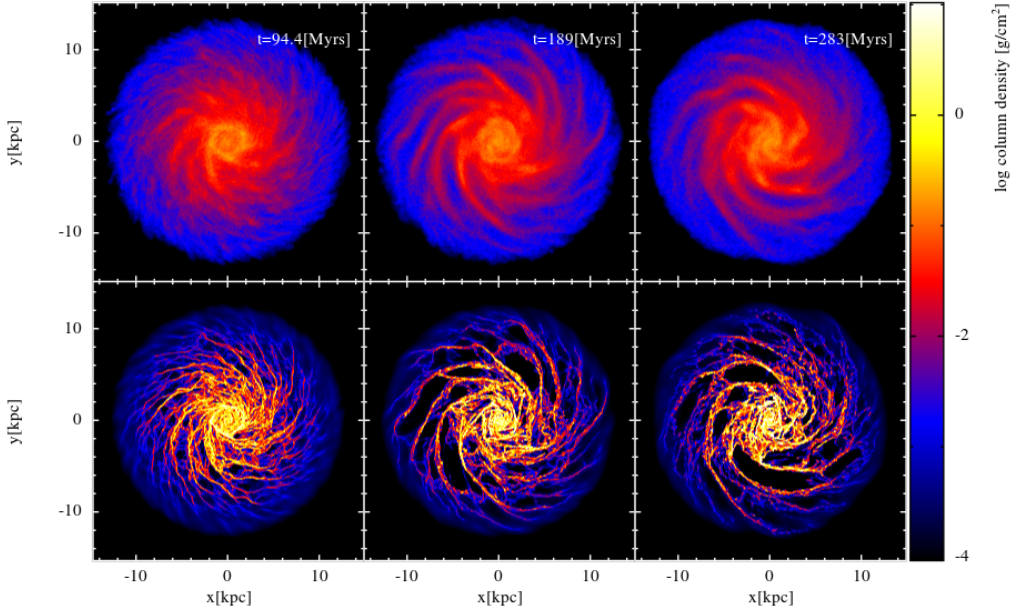


Figure 5.8: Evolution of a live stellar disc (top) and the accompanying gas disc (bottom) in the Dc model over 280Myrs. Clear spiral arms can be seen to grow with evolution of the disc.

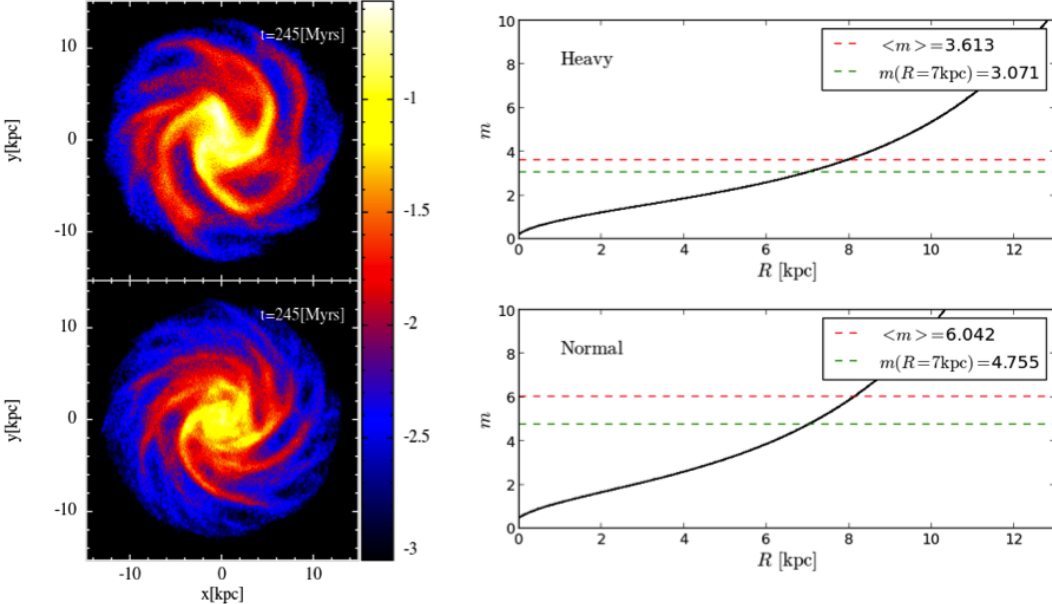


Figure 5.9: Top down views of two live disc simulations with different disc masses (Db top, Dc bottom) and their associated predicted swing-amplified modes as a function of radius (right panels). A Fourier analysis of the heavier disc model in the top panel gives a dominant arm mode of  $m = 3$  which is in agreement with that predicted in the mid-disc by swing amplification. Likewise the lighter disc has a dominant mode of  $m = 5$ , also in good agreement with the predicted value. The predicted mode is calculated via Equation 1.9 as a function of disc mass, epicycle frequency and radius.

the gas. By 200Myrs these features appear greatly diminished in Db and Dc, with a settled rotation curve, and so we do not analyse gas before this point.

In our two primary disc calculations, Db and Dc, there appears to be a good agreement between the number of arms formed and that predicted by swing amplification (Equation 1.9). In Figure 5.9 we show the Db and Dc models (stellar component only) in the left panels. By-eye it appears that the higher mass disc (top) has fewer individual arm features than the lower mass disc (bottom). In the adjacent panels we show the swing amplified mode predicted using the initial conditions of the gas disc. The mode increases with radius, but two useful values can be drawn, the average  $m$  over the entire disc, and the value at 7kpc (half-way and near the solar position). The values for these models predict a value of  $3 < m < 4$  from the Solar position to the edge of the disc in the Db (i.e. heavy) model, and  $4.5 < m < 6$  in the Dc model. We use the method of Section 5.3 to find the dominant arm mode, rather than assessing by-eye, and find values of  $m = 3$  and  $m = 5$  for the Db and Dc models respectively. These are in excellent agreement with those predicted in the outer disc, implying the swing amplification prediction allows for a rough estimate of resulting arm number. The pitch angle however gives extremely high values, with values of  $20^\circ$  and  $28^\circ$  for the Db and Dc models, far outside values inferred for the Milky Way and at the high end of values seen in external galaxies.

Due to the nature of the bulge-free system, the rotation curve for these models decays rapidly approaching the Galactic centre. As opposed to models with bulges, where the curve rises near  $R \approx 2\text{kpc}$ , keeping a near-constant rotation throughout the disc (see Fig. 5.2). This leads to the lack of an ILR, which has been theorised and seen in observations to encourage the growth of a bar in the inner disc (see Sec. 1.3.4 for a discussion). The model DbG, which we allowed to evolve for 1Gyr before the addition of gas, was found to display a clear bar structure. This bar is relatively short compared to that believed to persist in the Milky Way, with a semi-major axis of approximately 2kpc and fairly wide with axis ratio of approximately 2:1. In general, any disc model without an inner bulge formed a steady bar after around a Gyr of evolution, whereas systems with a strong inner bulge tended to be bar-free.

The evolution of such a bar is shown in Figure 5.10 for stars and gas (top and bottom panels respectively). This bar rotates at approximately  $\Omega_p = 28\text{km s}^{-1} \text{kpc}^{-1}$ , which is slower, but not outside of uncertainties, than that of the Milky Way. In this figure the bar can be seen to generate arm structure at its ends, though these eventually de-couple from the bar and dissipate, leaving new arms to form in their wake. These arms have a wide pitch angle in the inner/mid disc, with values of  $20^\circ$ - $28^\circ$ , however, the arms stray from a logarithmic spiral at the edge of the disc where they strongly circularise making fits to  $\alpha$  problematic. The model shown in the figure is of a lower resolution in the gas than the models presented in the rest of this chapter. There are only 0.1 million gas particles, as opposed to the fiducial 3 million. We show this model because we had tremendous difficulty maintaining the higher resolution models. The forcing time-step for the gas became detrimental to the computation time due to the effects of the gas entering and leaving the barred region.

Nevertheless, the gas in the low resolution run in Figure 5.10 can be seen to trace out the bar. In intermediate times the gas traces out a long line along the bar, tracing its major axis.

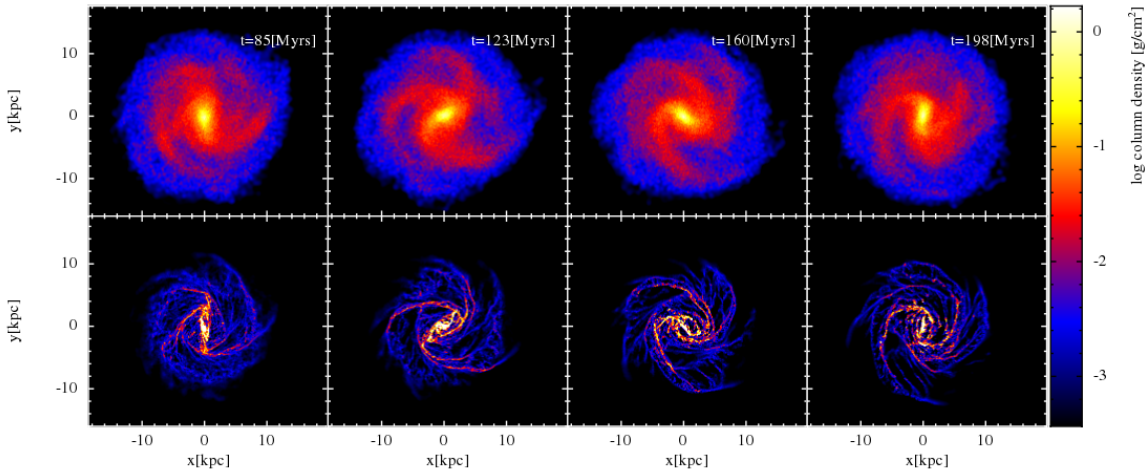


Figure 5.10: Evolution of a low-resolution disc with initial bar in the stellar disc. Shown for 200Myrs of evolution, where the bar has already been allowed to evolve for 1Gyr before inclusion of a gas disc. Stars and gas are in the left and right panels respectively.

No inner ring is seen as in the barred models of Chapter 3 due to the lack of any ILR. To assess the suitability of this model to the Milky Way we project the position of the gas particles into  $l$ - $v$  space. The resolution is too low to properly map the emission structure, but by simply re-mapping we can gauge the similarities to our Galaxy. In Figure 5.11 we show the gas distribution with the bar angled at  $\theta_b = 20^\circ$  and the corresponding projection of gas into  $l$ - $v$  space (the observer is at  $y = 8\text{kpc}$  in the top-down view). The second  $l$ - $v$  map shows the bar at a wider orientation angle ( $\theta_b = 50^\circ$ ). Some structures do seem similar to observations, such as arms features that resemble Carina and Perseus arms. However, in order to obtain an  $l$ - $v$  structure with features that resemble the Milky Way we had to lower the observers velocity to  $180 \text{ km s}^{-1}$ , well outside of our normal range. This is to compensate for the lack of a bulge, and generally shallower rotation curve in the inner disc compared to our other models. While the rotation curve has indeed risen in the inner disc since the start of the simulation thanks to the inner bar, it is still low compared to the values inferred from observations ( $V_c \approx 150 \text{ km s}^{-1}$  as opposed to the observed values of  $V_c \approx 250 \text{ km s}^{-1}$ ). While the creation of a bar is promising, we still require a bulge to match the velocity structure of our Galaxy, which inhibits bar formation (see next section).

#### 5.4.2 Live disc and bulge

The main Galactic disc configuration investigated is the Ba-d group of models, which contain a live disc and bulge, but maintain a static dark matter halo to reduce computational effort. We show the Ba, Bb, Bc and Bd models at three separate intervals in Figures 5.12, 5.13, 5.14 and 5.15 respectively. Stars are shown in upper panels, and gas in the lower. The third time frame of the Ba model is slightly earlier than the other models. This is due to the computation taking significantly longer than the others<sup>1</sup>. We did not continue this calculation further as maps made from existing

<sup>1</sup>Run time appeared to scale with stellar disc mass due to the size of the forcing time-step experienced by the gas particles entering from regions of very low to very high density.

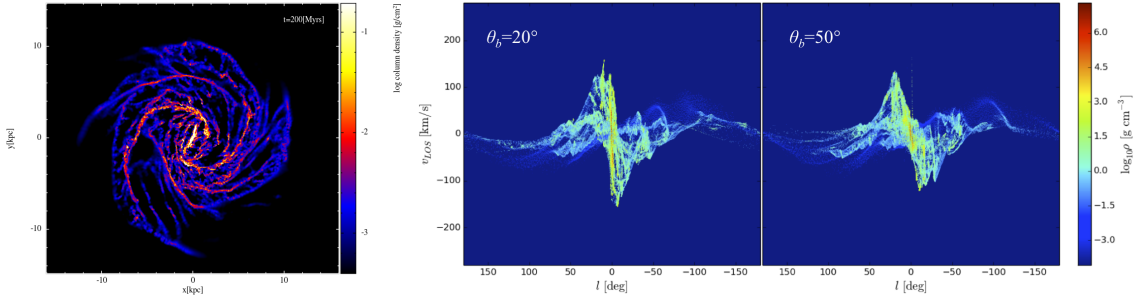


Figure 5.11: Gas embedded in a stellar disc after a bar has been allowed to form, and then evolved for 200Myrs with the gas. In the left panel the projection of the gas into  $l$ - $v$  space is shown for bar orientations of  $\theta_b = 20^\circ$  and  $\theta_b = 50^\circ$  (left and right respectively). The observer is placed at  $y = 8\text{kpc}$  and given a rotation speed of  $180\text{ km s}^{-1}$ .

time-steps and lower resolution calculations that had evolved for longer showed the Ba model was a poorer fit to Galactic  $l$ - $v$  data in general.

As with the disc-only models, the gas clearly traces the arm features in the stars. The higher density gas in the disc is the location of the majority of the molecular content. In the highest mass disc (Ba) there is very little inter-arm gas. In the arm cavities in Figure 5.12 there are effectively no gas particles, though stars are still present (seen by the non-zero density in the stars in the inter-arm regions). The gas is effectively being swept-up in an arm passage and is not released until the arm is sheared apart by rotation. The arms in the Ba model appear non-logarithmic in many places, especially so in the final panel. Various kinks, or knees, form along the spiral arms. The disc mass appears to be very large to be supported by rotation, and the stellar-gravity is producing strong local collapse into these irregular arm patterns. At the time of the middle panels of Fig. 5.12, Fourier analysis indicates that  $m = 2$  is the dominant arm mode with a wide pitch angle of  $20^\circ$ . This only persists for  $R < 9\text{kpc}$ , above which there is no clear dominant mode. At the latter time the  $m = 2$  mode still dominates at a similar pitch angle, but there is considerable power in the  $m = 3$  and  $m = 5$  spiral modes, visible by-eye. The pitch angle of the  $m = 2$  mode is maintained between the second and third panels of Figure 5.12 over which time the average pattern speed is  $\Omega_p = 38\text{ km s}^{-1} \text{ kpc}^{-1}$  ( $4 < R < 9\text{kpc}$ ). Interestingly the pattern speed here is fairly flat with radius, rather than decreasing.

The Bb model (Fig. 5.13) shows much more regular spiral structure, with some clear dominant spiral modes visible in the stars. There is also a moderate amount of inter-arm structure in the gas with features being continuously created and destroyed as arms are sheared out and re-formed. The pitch angle and pattern speed analysis for this model is used as the example in Section 5.3. The dominant arm mode (left, Fig. 5.4) appears to clearly favour a 2-armed pattern in the inner disc and a 4-armed in the outer. This is seen by inspection of the stellar distribution in Figure 5.13, where a small 2-armed feature can clearly be seen inside of  $R < 5\text{kpc}$  while the edge of the disc displays four arm tails. The Milky Way is also thought by some to have a higher arm number in the outer disc, and there is also confusion over whether there are 2 or 4 spiral arms (Amaral & Lepine 1997; Levine et al. 2006). The pitch angle of 4-armed pattern is approximately  $20^\circ$  and the pattern speed has a mean of  $25\text{ km s}^{-1} \text{ kpc}^{-1}$ , though this is seen to decay with radius;

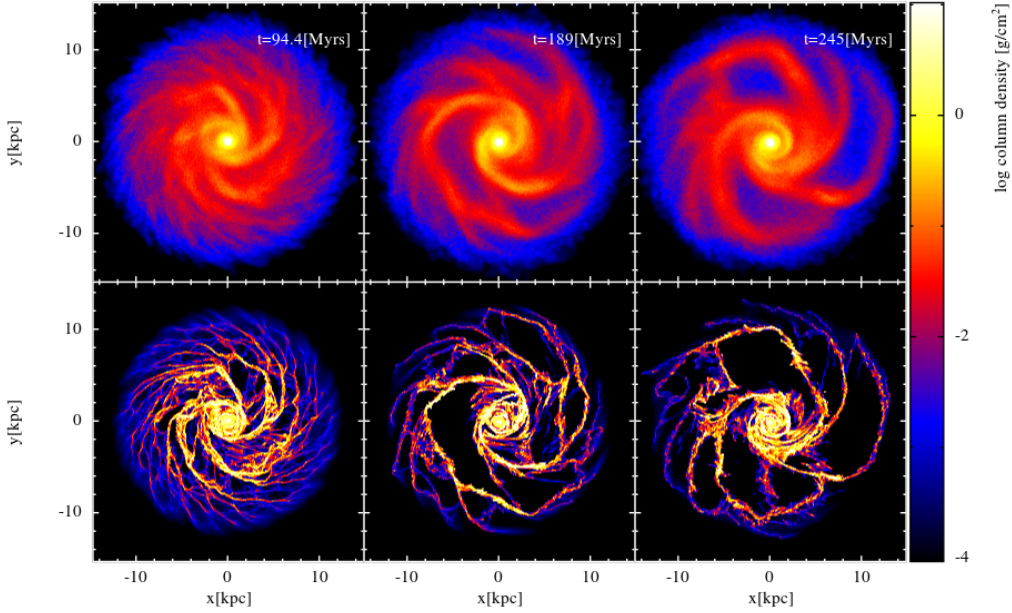


Figure 5.12: Evolution of the Ba model, with the heaviest disc mass investigated, in the stellar (top) and gaseous component (bottom). Large scale arm structures can be seen, yet appear rather irregular with many knee and kink features.

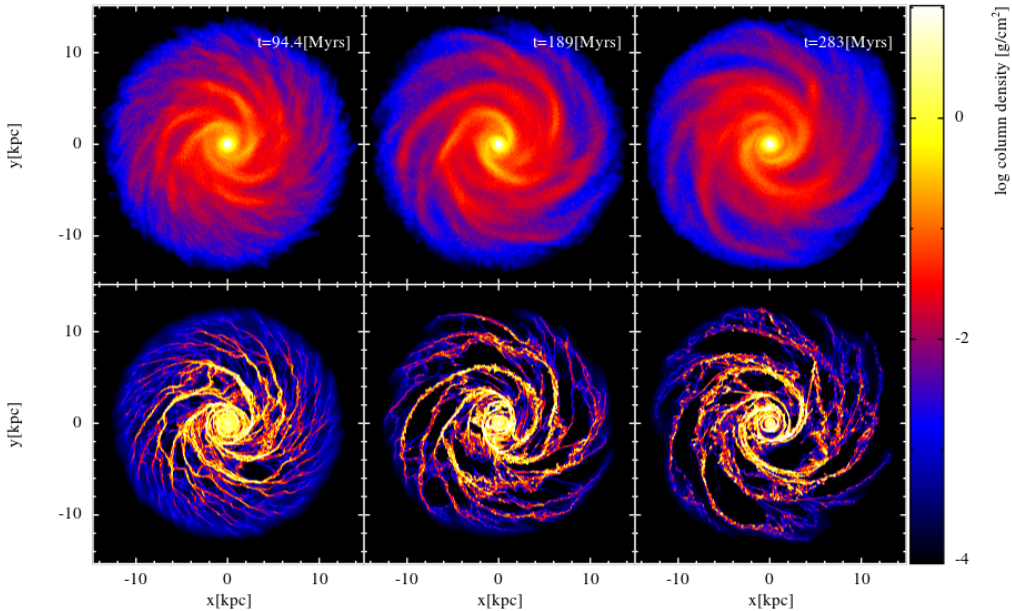


Figure 5.13: As Fig. 5.12 but for the Bb configuration. Arms appear more smooth and regular compared to the Ba model.

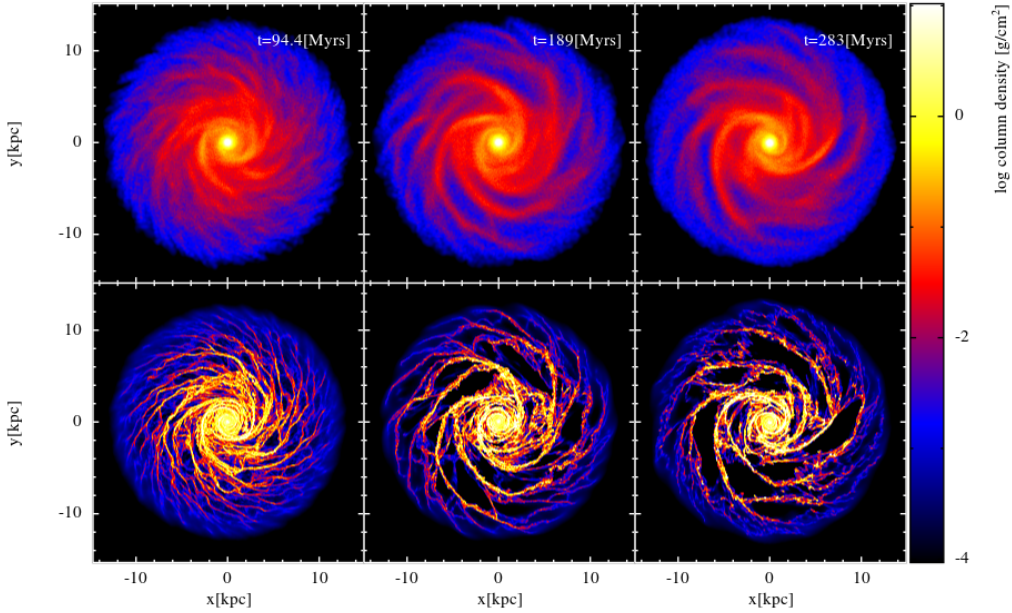


Figure 5.14: As Fig. 5.12 but for the Bc configuration. A significant amount of small arm structures are now visible compared to Ba and Bb.

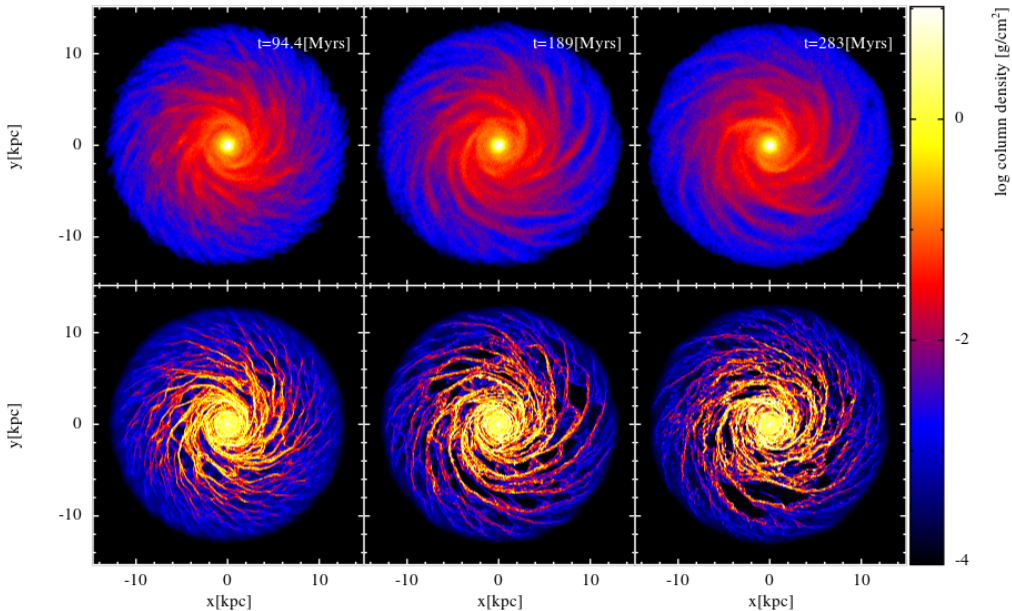


Figure 5.15: As Fig. 5.12 but for the Bd configuration. Arm structure is very small scale and flocculent with no clear dominant spiral mode visible by-eye.

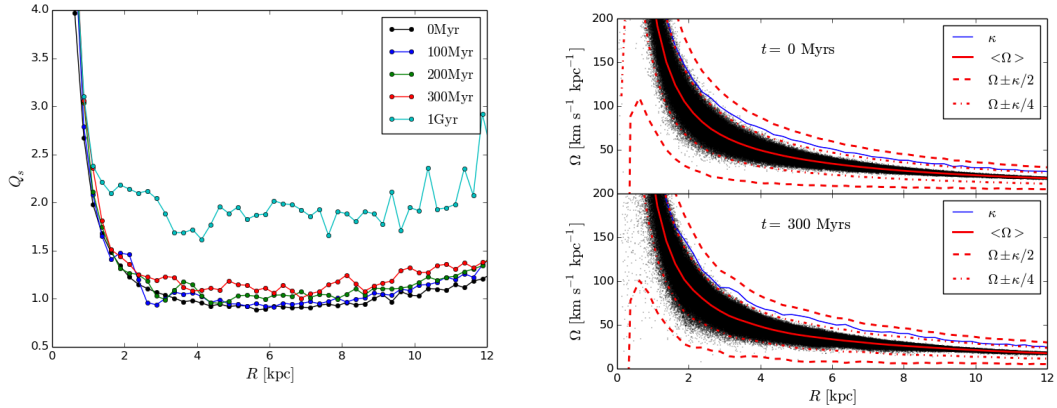


Figure 5.16: Evolution of the Toomre  $Q$ -parameter in the Bc disc-bulge calculation as a function of radius (left). In right panel the orbital frequency of gas particles is shown for the same model at initialisation (top) and after 300Myrs of evolution.

$20\text{km s}^{-1}\text{kpc}^{-1} < \Omega_p < 30\text{km s}^{-1}\text{kpc}^{-1}$  in the range  $4\text{kpc} < R < 11\text{kpc}$  indicating the arms are material in nature. If the arms are fit to the  $m = 2$  component inside  $R < 5\text{kpc}$  then a similar pitch angle is inferred than the  $m = 4$  case.

The Bc model in Figure 5.14 is similar to the Bb model, with some clear spiral features and inter-arm material. There also appears to be a 2-armed mode in the inner disc, though this is less clearly defined than the heavier case. When fitting to the spiral arm number there are two dominant modes;  $m = 4$  and  $m = 5$ . The latter is the strongest amplitude, but is a clear spike rather than being the prevalently strongest amplitude. Interestingly this spike occurs very near to the Solar position (7kpc) and gives a pitch of  $18^\circ$ . This is interesting as in many Galactic models the preferred structure is a 4-armed spiral, but with the addition of some small spur or minor Local arm which is always separate from the 4 main arms. The fact that the Bc model is preferentially a 4-armed model throughout most of the inner disc, lightly 2-armed in the centre, and seemingly 5-armed near the Solar radius makes it an excellent candidate for replicating Galactic  $l$ - $v$  features. The pitch angle of the  $m = 4$  mode is only slightly higher than the  $m = 5$  mode and displays a mean pattern speed of  $25\text{km s}^{-1}\text{kpc}^{-1}$  and a range of  $22\text{km s}^{-1}\text{kpc}^{-1} < \Omega_p < 35\text{km s}^{-1}\text{kpc}^{-1}$  which is at the high end of values calculated for the arms of the Milky Way.

The lightest model (Bd) is shown in Figure 5.15. Here there appears to be a clear departure from the Bb and Bc models in that there is no clear spiral mode visible by-eye. The structure of this disc appears to mimic a flocculent spiral galaxy such as NGC 4414 with multiple small scale arms and inter-arm features. Performing a fit to the arm features tends to reveal little more information. Across numerous time frames there is no clear mode that dominates more than a couple of kpc of the disc. There appears two spikes in amplitude, one for the  $m = 2$  mode in the inner disc, similar to the other models, and one for an  $m = 5$  mode at  $R = 8\text{kpc}$ . Beneath which is an indeterminate mess of amplitudes with  $m = 4$  and  $m = 6$  showing small scale peaks. Attempts to fit a pitch angle to the  $m = 5$  mode result in values in the range  $15^\circ < \alpha < 23^\circ$  and the pattern is impossible to determine with values ranging from  $20\text{km s}^{-1}\text{kpc}^{-1} < \Omega_p < 40\text{km s}^{-1}\text{kpc}^{-1}$  depending on the features incorporated into the fit.

Our final model of a bulge-disc system is shown in the left panel of Figure 5.17, where we have allowed the disc to evolve for 1Gyr before the addition of gas. The result is a disc that is very smooth, with no clear spiral features. Some very tightly wound arms appear in the gas, but these appear local in nature and are rapidly wound up and dispersed. At this stage the stellar disc is highly stable to perturbations, with  $Q \approx 2$  in the inner disc (the 1Gyr data in Fig. 5.16). The morphology of the gas is almost ring-like, with no bar or inner  $m = 2$  mode as in the previous calculations. It has been postulated that some other mechanism is needed to maintain spiral structure for 10's of galactic rotations in numerical simulations (Fujii et al. 2011). In the calculations of Sellwood & Carlberg (1984) additional forms of energy are added to maintain spirality, effectively imitating star formation, keeping the disc warm enough to maintain its spiral structure. D’Onghia et al. (2013) instead propose that the spiral structure can be continually re-seeded simply by GMCs perturbing an otherwise featureless stellar disc. Our simulations are fairly low resolution compared to pure  $N$ -body simulations in the literature. We saw in initial test calculations that arm features become weaker and short lived as the resolution is decreased, and so we do not expect them to last longer than the order of a Gyr.

We do not show any figures of the BbL model (lighter gas disc). The morphology is very similar to that of the fiducial mass disc (Bb). This model is used to primarily gauge the effect of disc mass on the CO emission features (Sec. 5.6).

### Disc stability

In all of the models presented above there is a lack of inner bar-like structure throughout. This is believed to be due to the  $Q$ -barrier caused by the inclusion of the bulge, which was absent in the disc only models. In Figure 5.16 we show the  $Q$ -parameter for the stars in the left panel as a function of radius. A clear incline can be seen near the galactic centre which acts as a boundary in stability, stopping waves from propagating through the centre (see Sec. 1.3.1). Interestingly all models show a trailing  $m = 2$  mode in the inner disc. It is possible this is the disc attempting to form a bar as in the disc models, but is undermined by the increased stability inherent to the bulge dominated region. If this were the case, then it implies there is some small region of parameter space where it is possible to form a bar but also maintain a rotation curve that is near-flat, presumably by considerably reducing the bulge mass. This stability of the inner disc against arm and bar formation also causes a small disc of molecular material at the galactic centre. In the gas density renders there is a disc of material of very high density inside  $R < 2\text{kpc}$  where molecular gas is easily maintained. This was very much not the case in the models with fixed potentials, where the bar, and arms in some instances, swept up the gas into steady orbits and left the very centre of the disc relatively devoid of gas.

The  $Q$ -parameter is a key quantity in determining stability. In the left of Figure 5.16 the evolution of  $Q$  is shown from 0-1Gyr. Initially  $Q \approx 1$  in the mid-disc, as expected from the setup conditions, making the disc barely stable. Over 300Myrs  $Q$  can be seen to slowly increase throughout the disc, raising to approximately 1.2 in the mid-disc region. At much later times, of the order of Gyr,  $Q \approx 2$ , implying the disc is highly stabilised. In the right panel the rotation frequencies for the stars initially and after 300Myrs are shown. The dashed lines show the resonance curves,

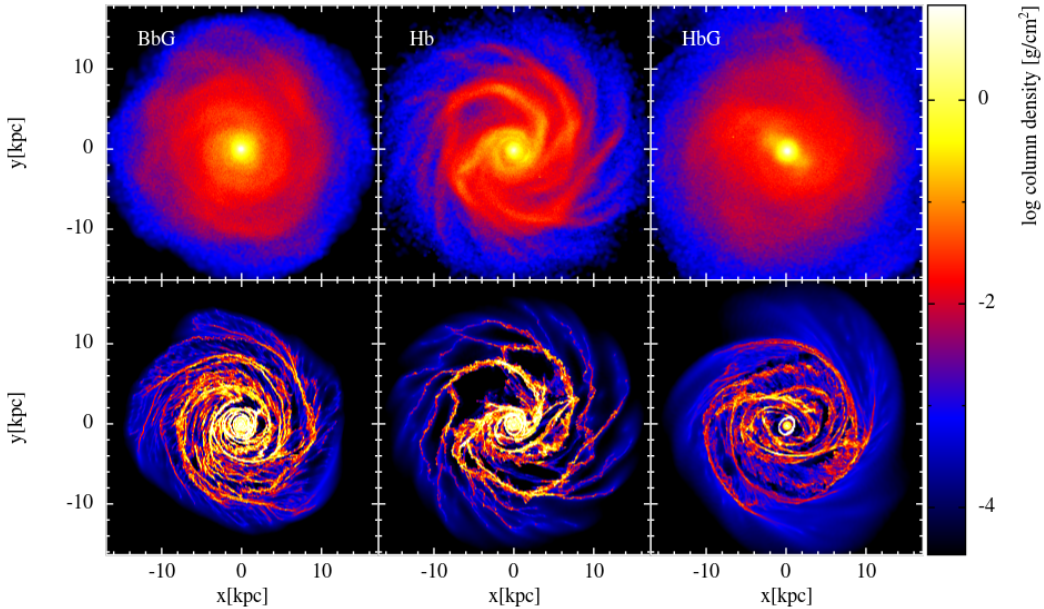


Figure 5.17: Stellar (top) and gas (bottom) densities in our three remaining models. BbG (left) has a much further evolved disc than those shown previously and the gas has formed many shallower pitch angled arms closer in morphology to rings. Hb (middle) has arm features not dissimilar to the static halo counter-part (Bb). HbG (right) has an evolved bulge-disc-halo system and has formed a bar in the centre, though weaker compared to that formed in the disc-only models. Only disc particles are plotted in the stellar density render. Note the HbG model is of slightly lower resolution, with only 1 million gas particles.

indicating the presence of the ILR and OLR. Note that the rotation structure is largely unchanged in the evolution of the system, with the main difference at later times being the existence of small scale fluctuations in  $\kappa$  (and hence resonances), presumably caused by asymmetries in the disc, i.e. arm features.

The rotation curve of each disc model showed a dispersion that increased with disc mass, both initially after several hundred Myr of evolution. Dispersion around the mean rotation curve ranged from  $\pm 50 \text{ km s}^{-1}$  in Ba to  $\pm 20 \text{ km s}^{-1}$  in Bd. The dispersion in the rotation curve therefore appears directly related to the number of arms formed, which is unsurprising as the dispersion is also incorporated into the value of  $m$  predicted by swing amplification ( $m \propto \Sigma^{-1}$ , and  $\Sigma$  determines the stellar velocity dispersion).

#### 5.4.3 Live disc, bulge and halo

For the basic live halo-disc-bulge models, the morphology is not dissimilar to the static halo models. In the central panel of Figure 5.17 we show the stellar (top) and gas (bottom) morphology in the Hb model after 240Myrs of evolution. The arm structure is quite asymmetric, with some clear branching features. There appears to be a dominant 2-armed pattern in the inner/mid disc, which dissipates in the outer disc. Fitting arms to this feature gives a pitch angle of  $\alpha \approx 20^\circ$ , similar to

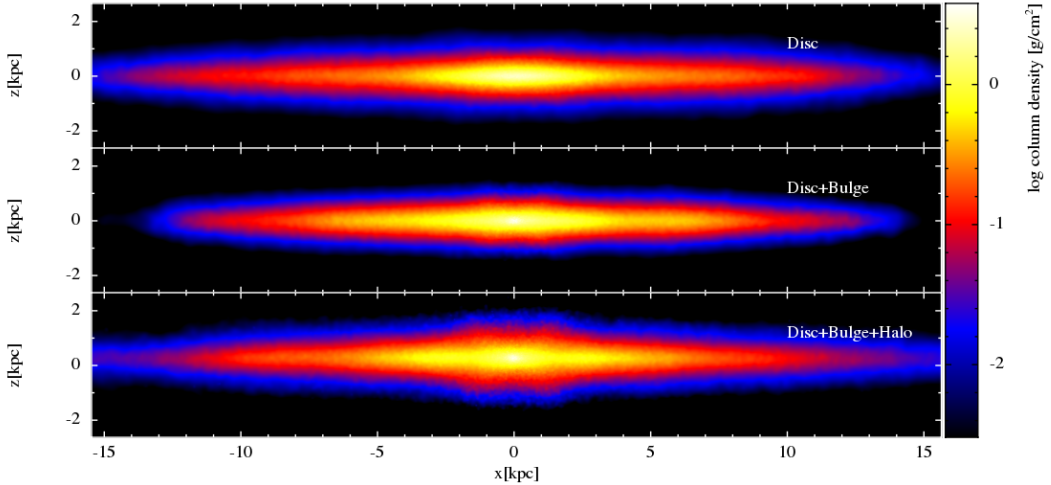


Figure 5.18: Vertical density render of the stellar distribution in three different simulations. In the top panel is a live disc calculation that had formed a bar (DbG), in the middle a live disc-bulge calculation with no bar (Bb) and in the bottom panel a live disc-bulge-halo calculation that formed a bar (HbG). Gas, bulge and halo particles have not been plotted for clarity.

values found in the previous models. There is a moderate strength  $m = 4$  mode in the outer disc with  $\alpha \approx 18^\circ$ , but this only dominates around  $R = 8\text{kpc}$ , and the fit to one of the four arms is very tenuous (evident from the top down view in Fig. 5.17). The pattern speed for the  $m = 4$  mode gives a high average of  $\Omega_p = 30\text{km s}^{-1} \text{kpc}^{-1}$ , but this is only valid for the very narrow radial range where the mode dominates.

The turbulent nature of the disc, and the irregular spirality, in the Hb model led us to perform the HbG model. Here the stellar system had been evolved for 1Gyr before the addition of the gas component. In the right panel of Figure 5.17 we show such a model after 260Myrs of evolution. An interesting development has occurred in this model. A weak bar has formed in the inner disc, with a strong spheroidal component, presumably owing to disc orbits interacting with the bulge. The density contrast between this bar and the surrounding disc is lower than that of the disc only simulations (Fig. 5.10). The gas response is extremely similar to that of the previous chapters where we utilised fixed analytic potentials for the bar (e.g. Fig. 3.13). There is a clear nuclear ring inside the bar, which did not exist in the disc-only models due to a lack of any ILR. Around which is a void of gas, and an oval-like set of orbits tracing the outer bar structure. Beyond which are a set of arms, which trail off the bar ends and wind up with rotation. The pitch is highly circular in the mid-outer disc. Tracking the motion of the bar gives a pattern speed of approximately  $\Omega_p = 45\text{km s}^{-1} \text{kpc}^{-1}$ , which is much higher than that of the bar in the disc only calculations. The OLR of such a bar occurs near 8kpc (see Figure 3.1b). If compared to the gas distribution in Figure 5.17 there appears a significant amount of substructure at this radius, which is similar to the features seen with static potentials. As with the disc barred model, the calculations at high resolution were severely hampered by the existence of the bar. The model shown in Figure 5.17 is the lower resolution calculation (1 million gas particles).

To further assess the nature of this bar we show the edge on appearance of the stellar disc

of the DbG, Bb and HbG models in Figure 5.18 (disc that formed a bar, bar-free disc+bulge and the bar formed in the live halo). The disc-only calculation is the narrowest vertically, appearing to not have changed much since the initial setup, despite the formation of a bar. The live-bulge calculation has a slightly flatter inner region compared to the disc only case, but the difference is marginal. Note the disc is greater extended radially compared to the other two as the disc is younger by around a Gyr, over which time the other models have expanded somewhat. In the live halo run, however, there is an inner lobed structure. This is similar to seen in observations of peanut/boxy bars in external galaxies and our own Milky Way (see the NIR image of the Milky Way in Fig. 1.15). The lobes appear to also be associated with the ends of the bar. In the figure the bar is oriented at approximately  $60^\circ$  to the line of sight, and as the bar is rotated to lie parallel to the line of sight (pointing out of the page) these lobes disappear, leaving just a bright central concentration. The bar orientation angle has to be very wide to see such lobes, with the  $60^\circ$  for the figure usually lying out of range of values determined for the Galaxy (but not always; de Boer & Weber 2014). The position of these lobes is strongly coupled to the bar length and the bar in these models is approximately 3kpc long, shorter than the Long bar (with a semi-major axis of around 4.5kpc). If we could increase the bar length in our model then the lobes in Fig. 5.18 would lead to a shallower bar orientation more in keeping with observations.

## 5.5 Simple kinematic longitude velocity maps

### 5.5.1 Method

As with Chapter 3, we must take into account the uncertainty in the observer's position and velocity by varying the parameters  $l_{\text{obs}}$ ,  $V_{\text{obs}}$  and  $R_{\text{obs}}$ . However, as the morphology is highly time-dependant, similar to the mixed models of Chapter 4, we must also test multiple time-stamps for each simulation. We choose to do so in the range of 200-320Myrs of evolution of the gas disc. This is enough time to allow the majority of the molecular gas to form (seen to be  $t \gtrsim 150$ Myr in Fig. 3.10) and for the disc to settle into a spiral pattern that will persist for up to a Gyr. The range in these parameters is the same as used previously (Table 3.2). Note that we must search the full range of  $l_{\text{obs}}$  values, as we cannot assume the disc is symmetric.

The method is the same as that described as in Section 3.6 with one small difference. As the gas in the simulation is less strongly associated with spiral arms, with some dense material shearing away from arms but maintaining a high molecular content, there is a chance that Equation 3.18 will scale poorly due to a clump of high density gas that lies very close to observing position. To rectify this we include a limiting factor,  $\epsilon$ , in the denominator to limit emission from material near the Solar position. This changes the equation for synthetic emission from Equation 3.18 to

$$I_{i,\text{synth}} \propto \chi_{i,\text{CO}} / (d_i^m + \epsilon) \quad (5.14)$$

where  $m$  is a factor to be determined (making  $\epsilon$  of dimensions  $\text{kpc}^m$ ). To find appropriate values of  $m$ ,  $\epsilon$  and the longitudinal smoothing length of emission (see Sec. 3.6 for meaning) we again constrain to a map created from the TORUS radiative transfer code. In Figure 5.19 we show the fit

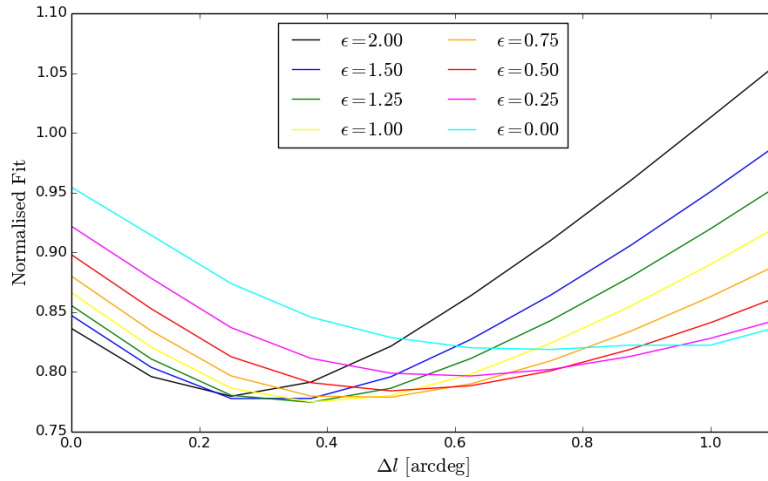


Figure 5.19: Best fitting values for the smoothing parameter ( $\Delta l$ , x-axis) and scaling limit factor ( $\epsilon$ , different coloured curves) when fitting a simple  $l$ - $v$  map to one created by TORUS. Best-fitting values are  $\epsilon = 1$  and  $\Delta l = 0.40^\circ$ , with the corresponding map and TORUS map shown in Figure 5.20.

statistic (MAE) from fitting to the  $\epsilon$  (coloured lines) and  $\Delta l$  (x-axis) parameters. The yellow line in the figure provides the best fit to the TORUS map, giving  $\epsilon = 1.0$  and  $\Delta l = 0.4^\circ$  (3 pixels). We maintain  $m = 2$  from the previous section, finding it to be an equally good fit as previously (not shown). Interestingly the longitudinal smoothing parameter is somewhat smaller than the value when using analytic potentials presumably because the dispersion in the star particles already acts to smear out emission in some way, whereas much of the gas lies confined in the bottom of the potential wells when using potentials. The resolution in the gas is also somewhat lower here (3 instead of 5 million) which can also have an effect.

The corresponding best-fitting map for these values of  $m$ ,  $\epsilon$  and  $\Delta l$  is shown in Figure 5.20 (top) along with the TORUS CO map to which it was constrained. General features and emission scale is similar in both maps, though again there are some subtle differences. The gas seems over smoothed in the simple map. We tried a fit to observer's position using this and a slightly narrower smoothing, and the minima for  $l_{\text{obs}}$ ,  $V_{\text{obs}}$  and  $R_{\text{obs}}$  were found to be the same, implying this is of little consequence.

We reiterate that these maps are not to be used for a quantifiable comparison to observations, merely to fix some additional parameters before continuing with analysis, and allow a fast sweep through the many possible maps. Once best-fitting values of  $l_{\text{obs}}$ ,  $V_{\text{obs}}$ ,  $R_{\text{obs}}$  and time-stamp  $t_{\text{bf}}$ , have been found for each model, we then use these to create TORUS data cubes of emission.

### 5.5.2 Maps of models

As an example of the fitting process to find the best fitting values of  $l_{\text{obs}}$ ,  $V_{\text{obs}}$ ,  $R_{\text{obs}}$  and  $t_{\text{bf}}$  we show  $l$ - $v$  maps for the Bb model in Figure 5.22, across multiple time-frames spanning  $200 < t < 300$  Myrs. The behaviour of the fit statistic is shown in Figure 5.21 as a function of  $t$ ,  $V_{\text{obs}}$  and  $R_{\text{obs}}$  where each point corresponds to a map in Figure 5.22. The red point indicates the best-fitting map

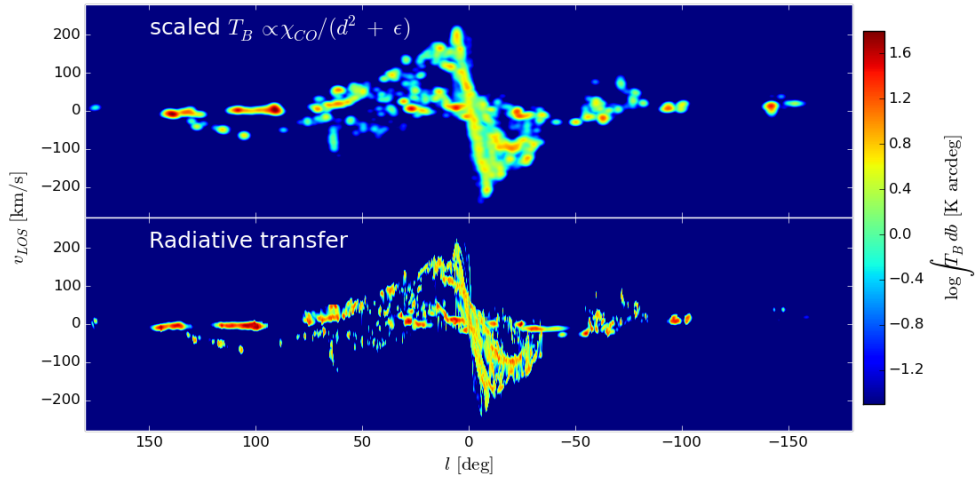


Figure 5.20:  $l$ - $v$  maps made using the simple method outlined in the main text (top,  $\epsilon = 1$ ) and using the TORUS radiative transfer code (bottom). The simulation contains a live bulge and disc component, and the observer is placed at  $R_{\text{obs}} = 7\text{kpc}$  with  $V_{\text{obs}} = 200 \text{ km s}^{-1}$ .

(values indicated at the top of the figure). In this example a clear minima is seen in the fit statistic for the 226Myr time-stamp, with associated values of  $V_{\text{obs}} = 200 \text{ km s}^{-1}$  and  $R_{\text{obs}} = 8.5\text{kpc}$ . The  $l_{\text{obs}}$  parameter is not shown, as it contains little information without some clear reference point such as in barred simulations. The best-fit map in Figure 5.22 shows features that mark it out from the others, such as the Carina arm being correctly placed. The fit seems to worsen at later times. Inspection of the corresponding  $l$ - $v$  maps indicates this is likely due to the inner disc material moving away from the position of the Inner Ridge seen in observations.

The process of fitting to  $l_{\text{obs}}$ ,  $V_{\text{obs}}$ ,  $R_{\text{obs}}$  and  $t_{\text{bf}}$  was performed for each model, with the exception of the DbG model which had not evolved sufficiently to show any features in the outer disc. The resulting best fit  $l$ - $v$  maps are shown in Figure 5.23 with parameters for each model given in Table 5.3. The disc models (Db, Dc) have some of the poorest fit values, which appears to be due their lack of emission at high velocities in the inner disc. Some arm structures are seen in the outer disc, but these do not stray far from the local velocity ( $v_{\text{los}} \approx 0 \text{ km s}^{-1}$ ). The halo model that had formed a bar (HbG) seems to produce no emission in the outer galaxy at all, implying the spiral features seen in the top-down maps are too weak. This is similar to the analytic bar models, where outer arms rarely extended into the outer disc, and if they did were found to be too weak. The inner nuclear ring in this model produces a very strong feature in  $l$ - $v$  space which is a strong function of bar orientation. For the best-fitting arrangement shown here the bar is angled at approximately  $\theta_b = 50^\circ$ , similar to the values found in the previous chapters.

The remaining models, all with a live bulge component, provide a variety of  $l$ - $v$  features. The heaviest disc model appears too turbulent in the inner disc. While it has an inner structure that is aligned similarly to observations, there is a large amount of material at high velocities and not matching the observed features. Coupled with the irregular arm structure seen in the top-down map, we conclude this (our heaviest disc) is a poor match to the Milky Way and do not produce any full radiative transfer  $l$ - $v$  maps. Moderate-to-light mass discs (Bb, Bc, Bd, BbG and Hb) provide

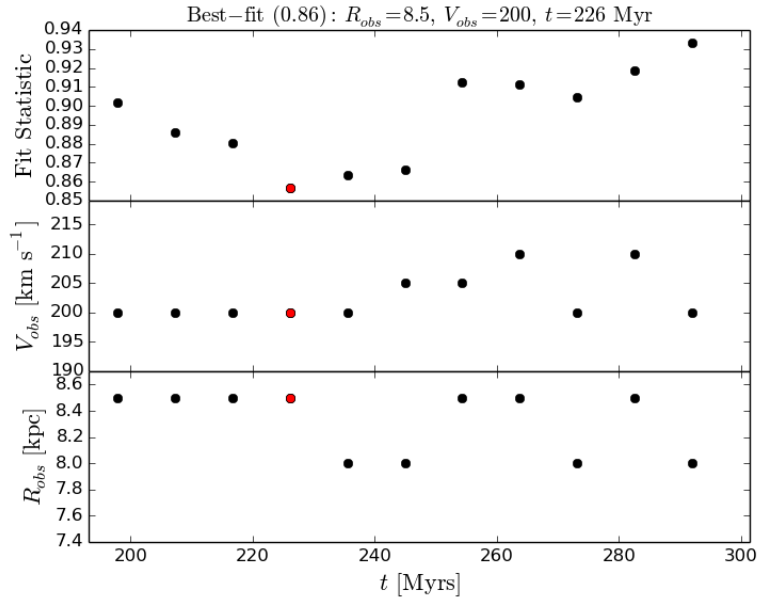


Figure 5.21: Variation of fit statistic with  $t$ ,  $V_{obs}$  and  $R_{obs}$  for the Bb model. The best fitting time-frame is indicated by the red point, with values given at the top of the Figure. Corresponding  $l$ - $v$  maps for each point are shown in Figure 5.22.

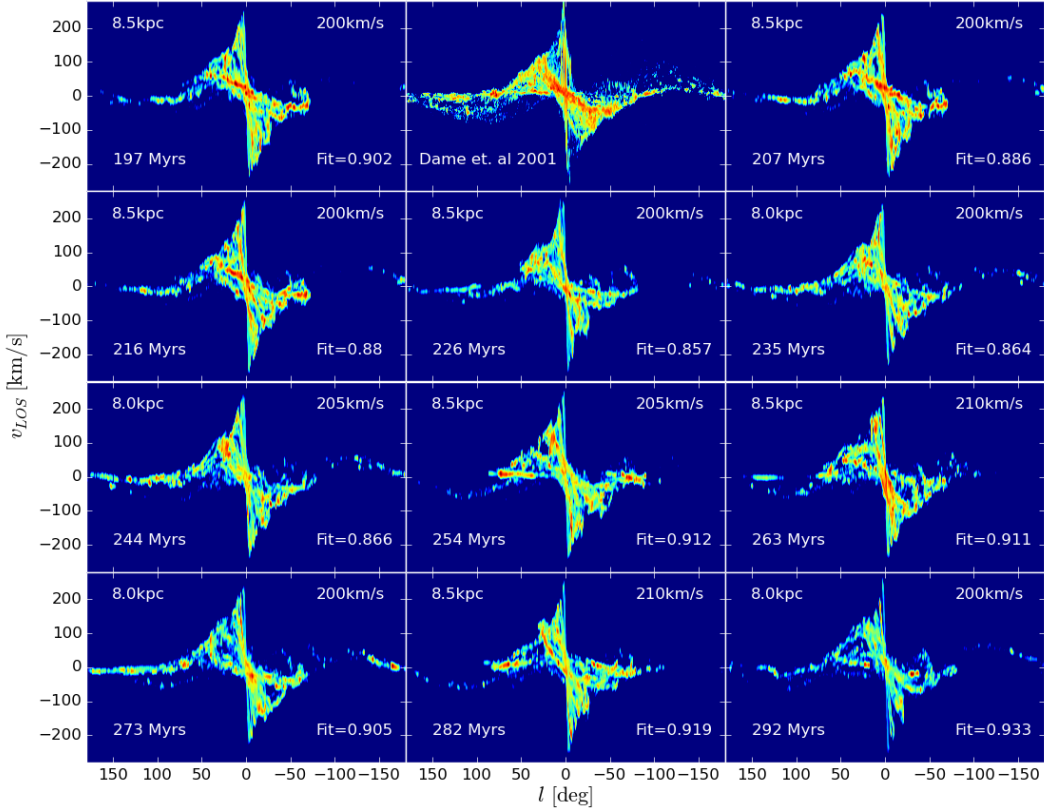


Figure 5.22: Evolution of kinematic  $l$ - $v$  maps for the Bb model where each panel has been fit to the map of Dame et al. (2001) to find the best fitting values for  $l_{obs}$ ,  $V_{obs}$  and  $R_{obs}$  which are indicated in each panel. Each panel corresponds with a point shown in Figure 5.21. Top centre is the CO observational data for comparison.

Model	$t_{bf}$ [Myr]	$R_{obs}$ [kpc]	$V_{obs}$ [km s $^{-1}$ ]	$N$	$\alpha$ [ $^{\circ}$ ]	$\langle \Omega_p \rangle$ [km s $^{-1}$ kpc $^{-1}$ ]	Fit stat.
Db	235	8.5	200	3	27	N/A	0.974
Dc	216	8.0	200	5	28	N/A	0.931
Ba	197	8.5	215	2	23	38	0.994
Bb	226	8.5	200	4	18	25	0.857
Bc	207	7.0	200	4	22	25	0.833
Bd	207	7.0	205	5	25	20-40 $^{\dagger}$	0.768
BbG	216	8.0	200	3	13	35	0.879
Hb	216	8.0	205	4	26	30	0.925
HbG	197	7.0	200	2	8-25 $^{*}$	N/A	1.086

Table 5.3: Results of fitting to  $l_{obs}$ ,  $V_{obs}$ ,  $R_{obs}$  and  $t_{bf}$  for each model and the corresponding arm models fit. The mean pattern speed across the disc,  $\langle \Omega_p \rangle$ , is quoted as in many cases the pattern speed was a function of radius.

\* Arms are strongly wound around a bar and do not trace a logarithmic structure well

$^{\dagger}$  Arm pattern is too flocculent to constrain rotation speed

a better agreement (and lower fit statistics). The lightest disc produces a near-uniform emission structure in the inner disc due to the flocculent nature of the arms. The Bb and Bc models provide good representations of the Carina and Local arms, while producing an Inner Ridge of the correct orientation. The remaining disc model, BbG, has good outer disc features but has an inner structure that reaches too high velocities. This could be due to the relatively low value of  $V_{obs} = 200$  km s $^{-1}$ , but this is needed to correctly place the Perseus arm. The inner feature of this model also appears straight in  $l$ - $v$  space, as opposed to the other models where the feature curves as it moves into the fourth quadrant. This is because arm features in this model are closer in morphology to rings than to arms (left, Fig. 5.17) which show up as straight lines in  $l$ - $v$  space.

The values in Table 5.3 show that models with the lowest fit statistic ( $< 0.9$ ) have a high arm number ( $3 < N < 5$ ). This implies the Milky Way emission features are best-fit by a high arm number, rather than the  $m = 2$  value as implied by some studies. Interestingly we had some difficulty producing  $N = 2$  armed structures. In the case of the Ba model the arms were highly irregular and appeared to be buckling in the outer disc, beyond the Solar position. The HbG model displayed a  $N = 2$  pattern, but these arms are trailing from the bar ends and do not extend far radially.  $N = 2$  arm models have been produced by studies in the literature, but tend to only be so when perturbed by some external body (Dobbs et al. 2010; Struck et al. 2011).

Pitch angles tend to be around  $\alpha \approx 20^{\circ}$ . While high, this is not outside of the uncertainties in Milky Way models. Values as high as these were ruled out when using fixed potentials because there appeared to be voids of gas in the disc due to the large arm separation, which provided a poorer representation of  $l$ - $v$  features. However, when using a live disc there is a considerable amount of branches and inter-arm material, which allowed for the arms to fit to additional structures in  $l$ - $v$  space. We estimate an uncertainty of around  $2^{\circ}$  for  $\alpha$ , gauged by varying the extent of the disc and material (gas or stars) used in the arm fit.

The pattern speeds in Table 5.3 have large uncertainty, and are only mean values as the pattern speed is seen to decrease with radius in all disc models. Regardless, the arm pattern speeds appear high compared to values inferred for the Milky Way and found when using analytic poten-

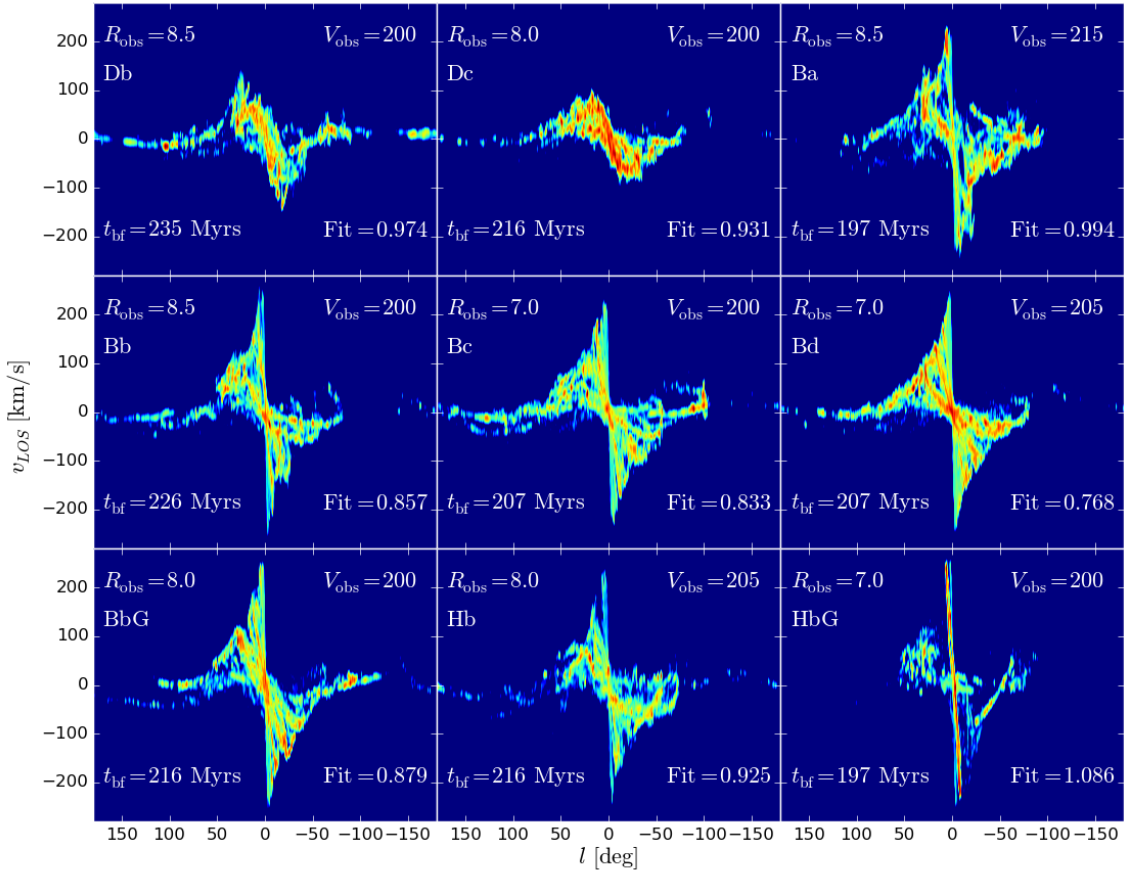


Figure 5.23: Best fitting  $l$ - $v$  from the simple fitting procedure to find  $l_{\text{obs}}$ ,  $V_{\text{obs}}$ ,  $R_{\text{obs}}$  and  $t_{\text{bf}}$  for models Db, Dc, Ba, Bb, Bc, Bd, BbG, Hb and HbG. Best fitting values are given in each panel, along with the value for the fit statistic used to constrain them.  $V_{\text{obs}}$  and  $R_{\text{obs}}$  are in  $\text{km s}^{-1}$  and kpc respectively.

tials ( $\Omega_{sp} \approx 20 \text{ km s}^{-1} \text{ kpc}^{-1}$ ). Values for bars lie between  $30 \text{ km s}^{-1} \text{ kpc}^{-1} < \Omega_p < 45 \text{ km s}^{-1} \text{ kpc}^{-1}$ , though we could not perform any barred simulation at high resolution for more than 90Myrs due to computational difficulties. The best fitting radius,  $R_{\text{obs}}$  varies across the models, with no clear preferred value. For instance the Bb and Bc models, which both provide a good match to the  $l$ - $v$  data, have best-fitting values of 8.5kpc and 7.0kpc respectively. The best fitting observer velocities appear systematically lower than those of the analytic potentials and the approximate value for the Solar position ( $220 \text{ km s}^{-1}$ ). We believe this to be due to the nature of the density distributions used to set the stellar material being slightly different to those of used in Chapter 3. By comparing the model rotation curves of Figures 5.2 and 3.1 at the Solar radius ( $R \approx 8 \text{ kpc}$ ) the models in this chapter appear to pass through the data points of Sofue (2012) in the Bd, Bc and Bb models whereas the model from Chapter 3 appears to over-estimate the local velocity by  $10 - 20 \text{ km s}^{-1}$ . As such, to match the velocity of local material the value of  $V_{\text{obs}}$  can be somewhat lower, in keeping with the rotation curve of the live stellar disc. The exception is the Ba model, whose rotation curve also over-estimates the local velocity, hence the higher best-fit value for  $V_{\text{obs}}$  (Table 5.3).

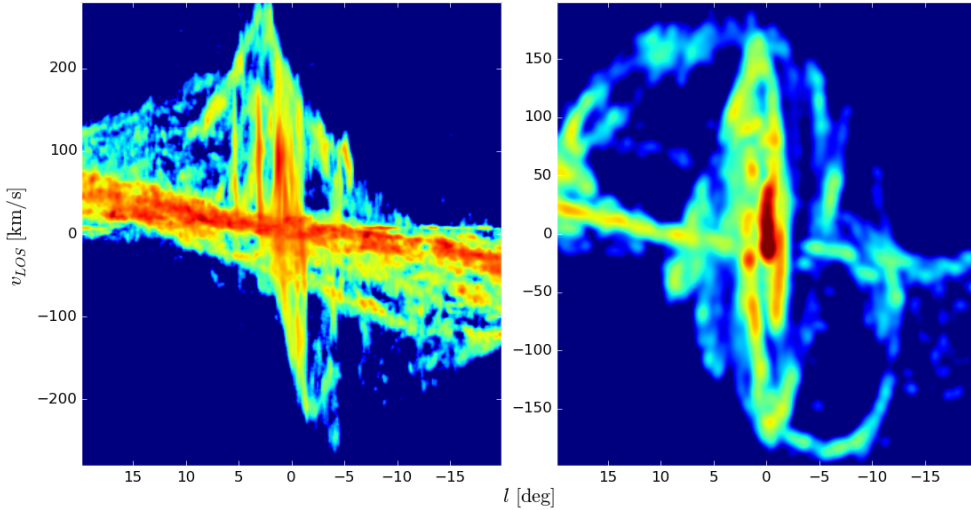


Figure 5.24: Inner structure of the gas disc in the DbG model (right) due to the creation of a bar, angled at  $\theta_b = 45^\circ$ . Features are similar to those seen in observations (Dame et al. 2001, left). Note the velocity range is slightly smaller in the right panel.

We have not shown any values or maps for the BbL model as they are extremely similar to those of the Bb model, with only slight variations in the best fitting values of  $l_{\text{obs}}$ ,  $V_{\text{obs}}$  and  $R_{\text{obs}}$ .

Regarding the barred models specifically, we do not perform any radiative transfer calculations using these models. They are either too low resolution, or did not run for long enough to develop sufficient structure. There is one point of merit we wish to discuss however. In the bar formed in the DbG model, that had only ran for 85Myrs with gas, there is internal structure that is very similar in  $l$ - $v$  space to that observed in CO data. The internal structure is shown in Figure 5.24 (right) alongside that seen in observations (left). The bar is angled at  $\theta_b = 45^\circ$  and the synthetic  $l$ - $v$  map is shown over slightly narrower velocity range (remember that without a bulge, disc-only models underestimate the velocities in the inner disc). While by no means a perfect reproduction, this is perhaps the closest to the CMZ out of all of our models. In both maps there is a bright vertical inner region that has a width of several degrees, with some emission structures falling away from the peak values as you move away from  $l = 0^\circ$ . The structures directly around the CMZ in the model appear at too high velocities, indicating the structure may extend too far radially, which could be reduced with the addition of a more compact inner bulge. Different values of  $\theta_b$  were investigated, but none lessened this effect. This model has the obvious drawback however of having very weak outer arms, though higher resolution calculations, where arms should be more prominent, were not feasible.

## 5.6 Radiative transfer emission maps

Using the methods discussed we have narrowed down the full range of models in Table 5.2 down to seven that we wish to analyse further and create emission maps, now taking into full account optical depth effects. These models are the majority of the bulge-disc calculations (Bb, Bc, Bd,

BbG, BbL) and a single live halo model (Hb). However, in instances of fitting the simple  $l$ - $v$  maps there were some double-minima seen in the fit which gave a considerably better match than the other models. Specifically we have included another Bc time-stamp, which is taken at a much later time (292Myrs, rather than the 207Myrs of best fit model) and provided a better fit than the Bd and Hb models. Some other instances such as this occurred, but none so clearly a good fit.

The procedure for creating  $l$ - $v$  emission maps is identical to that outlined in Section 4.3. We use the TORUS radiative transfer code to create cubes of brightness temperature as a function of latitude, longitude and line-of-sight velocity which are the integrated over latitude and quantitatively compared to the CO map of Dame et al. (2001). A turbulent velocity of  $4 \text{ km s}^{-1}$  is again added to the line width to better match the observed features. Sinks and stars are all discarded before the creation of maps.

### 5.6.1 Column densities

In Figure 5.25 we show typical column densities as a function of latitude and longitude in the second quadrant of a live-disc calculation, which can be directly compared to the fixed potential case (Fig. 4.6). The disc has been aligned such that similar arm structures are present, with a near, mid and far arm are all present in the quadrant. The near arm appears clearly as an emission feature that is vertically extended up to  $b = \pm 2^\circ$ , similarly to the fixed potential case. The remainder of the material is somewhat different. There is no clear narrow band of material centred at  $b = 0^\circ$  as for the fixed potential, with instead column densities appear well distributed with latitude. This is because the live stellar disc has a great many more homogeneities, and the vertical velocity dispersion in the disc keeps material away from the mid-plane which was a drawback of the previous models. The H I appears very uniform with no strong asymmetries or over-densities. Peak values of H I density are much lower than the fixed potential case, presumably because of the increased dispersion around the mid-plane. Molecular gas densities are similar however, as the densest gas is limited in molecular abundance by limiting factors (e.g.  $\chi_{\text{CII}}$ ) while the general gas density can continue to increase. Material is still confined to lower latitudes than that seen in our own Galaxy, where molecular and atomic gas can be seen to extent out to  $b = \pm 5^\circ$  (Heyer et al. 1998; Taylor et al. 2003). Stellar feedback may be necessary to produce this extended vertical structure (Duarte-Cabral et al. in preparation).

The molecular column densities for this quadrant are shown in Figure 5.26, to be compared with similar plots for fixed potentials (Fig. 4.8). These appear to give a poorer representation of the column density profiles in observations compare to those of Fig. 4.8. This could be due to the CO is being under-produced with respect to H<sub>2</sub> in comparison, though this seems unlikely as the chemistry for both codes is identical. It is possible that this is a resolution effect, and that the slightly higher resolution of the fixed potential calculations allowed for a greater resolution of the denser regions, more accurately following the molecular content in these regions (5 million as opposed to 1 million particles). The other possibility is that the dense gas regions inside these live disc calculations are less efficient at creating and/or shielding molecular gas compared to smooth potentials. This may be because these transient arms are not as consistently strong as the analytic potentials and that their transient nature is disruptive to the presence of molecular gas. The column

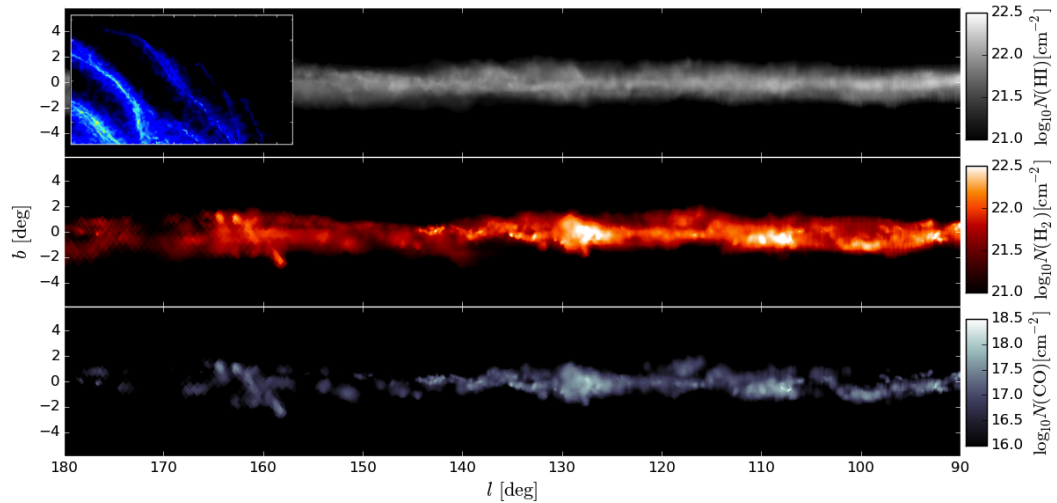


Figure 5.25: Column density of H I (top), H 2 (middle) and CO (bottom) of the second quadrant of the Bc model, shown in the insert.

densities do however provide one improvement to those of the fixed potentials. They have column densities that reach into much lower H 2 densities. The fixed potential data by comparison decayed very rapidly around  $N(\text{H}_2) \approx 10^{20} \text{ cm}^{-2}$ .

### 5.6.2 Emission maps

We show all seven of our best-fitting CO emission maps in Figure 5.27, and the observational data alongside for comparison. The fit statistic has been re-calculated now that the emission correctly takes into account emission and absorption effects, and correctly computes the “size” of the features. Encouragingly, the fit statistic follows the same trends across the maps as when we used the simple map creation tool. The three best fitting maps (in order) are the Bd, Bc (both) and Bb models. The BbG and Hb models fair significantly poorer in comparison.

The lighter gas disc is now shown (BbL) where the gas had half the fiducial mass. The emission features are significantly weaker than the Bb counterpart. While the strength of the emission is weaker over-all, more in line with observational values, there are clear gaps in  $l$ - $v$  features that are not present in the Bb model. We conclude that the fiducial disc mass (or somewhere between) is a better value for reproducing emission features.

While each model still has merits, there are clearly three that can be dropped from analysis: the BbL model (as stated above), the Hb and BbG models. The evolved disc model (BbG) provides a good reproduction of the Carina arm, Perseus arm and some of the Local arm. The inner disc however, is poorly reproduced. The inner ridge feature is angled too steeply in  $l$ - $v$  space, and seems to be tracing the ring-like inner structure of the disc rather than spiral arms. The lack of a full Local arm, or any Outer arm feature, also undermine this model. As expected the live-halo model (Hb) is similar to the static halo case (Bb). There is some marginal outer arm emission and a seemingly complex inner structure, though this appears more complex in the Hb model. Overall the Hb model is a poorer version of the Bb model, with weaker arm features, a misshapen

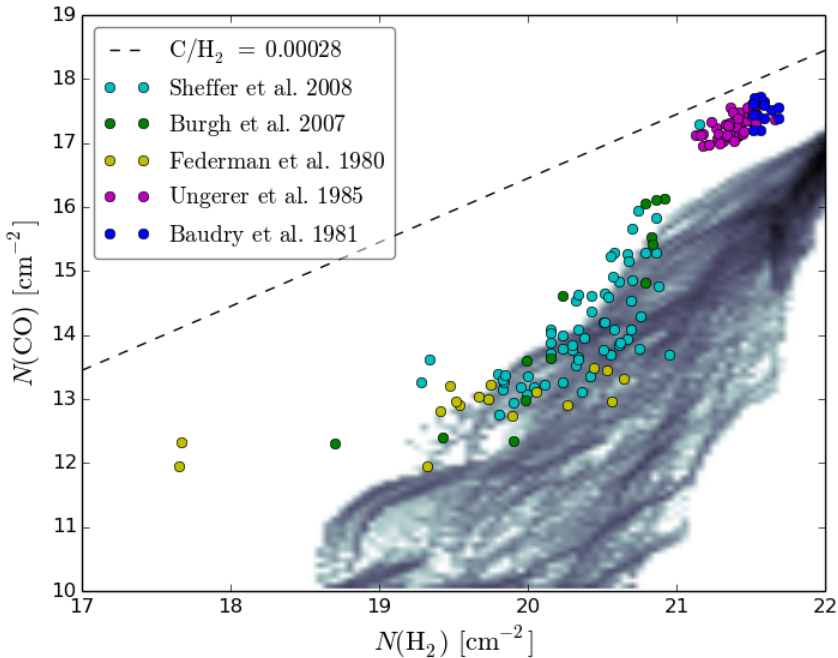


Figure 5.26: Column density of  $\text{H}_2$  and CO for the second quadrant of the Bc calculation shown in Figure 5.25. Several sources of observational data for the second quadrant are shown for comparison.

inner structure, poor reproduction of the Carina arm and poorer fit statistic. This could be due to additional dynamical instability possibly seeded by an unresolved dark halo so we don't consider this model further.

The remaining four models; Bb, Bc( $\times 2$ ) and Bd, all provide a good fit to many of the observed features. All produce the Carina, Perseus, and Local arm material, though some better than others. For instance, the lightest disc model appears to show extremely weak arm structure that can be assigned to Perseus, but it is barely visible in the second quadrant. The Inner Ridge is well produced in the Bc(292Myr) and Bd models, and in the case of the former this smoothly transitions into the Carina arm. The Fourier analysis of these models favours a 4-arm fit (5 for the lightest case), indicating that Galactic structure is best fit by a higher arm number, rather than say a 2-armed one.

So far we have limited ourselves to discussing the emission structures seen in CO. We provide a single map of the HI emission for comparison, using the Bc(207Myr) model. The emission here is a much better representation of that observed (lower panel, Fig. 5.28) than the fixed potential calculations. The arm structures are traced by the emission, similarly to the CO (Fig. 5.27) though there are many more weaker arm features visible. This is very different to the analytic potentials, whose emission structure did not show any strong correlation to the location arms and CO emission for our standard surface density (Fig. 4.3). This is likely because the gas is less confined to the plane when using a live disc, and so it decreases the optical depth and hence HI absorption along lines-of-sight to the arms. The emission strength is also comparable to observed values, with peak emission features appearing near 200K. The structures here appear very fine

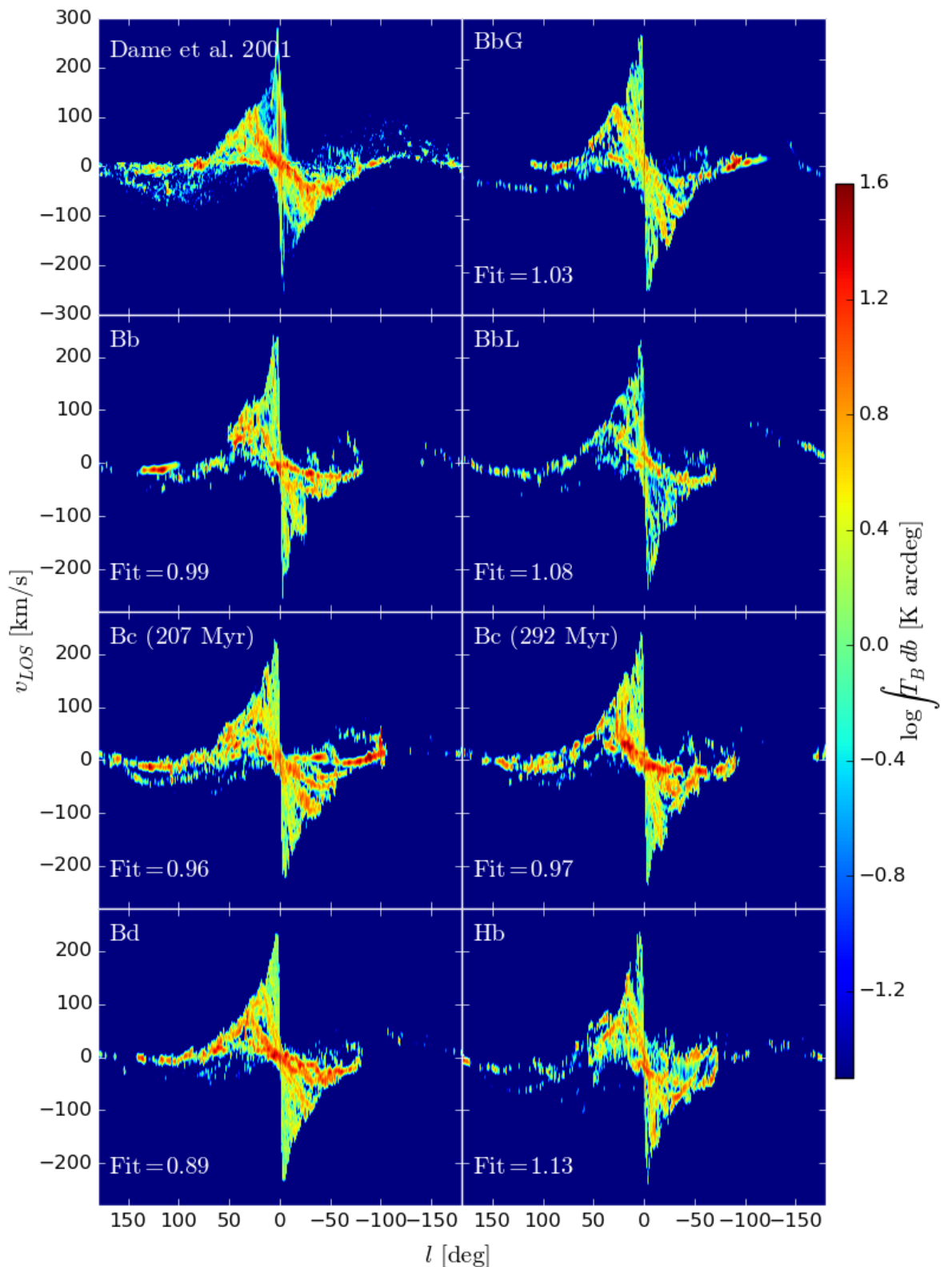


Figure 5.27: Seven CO emission maps made using TORUS where time-fame and observer coordinates have been fitted to observational data (top left for comparison, re-scaled slightly to match synthetic maps). The models include the Bb, Bc, Bd, BbL, BbG and Hb mass configurations, and an additional Bc that also provided a good match to the data.

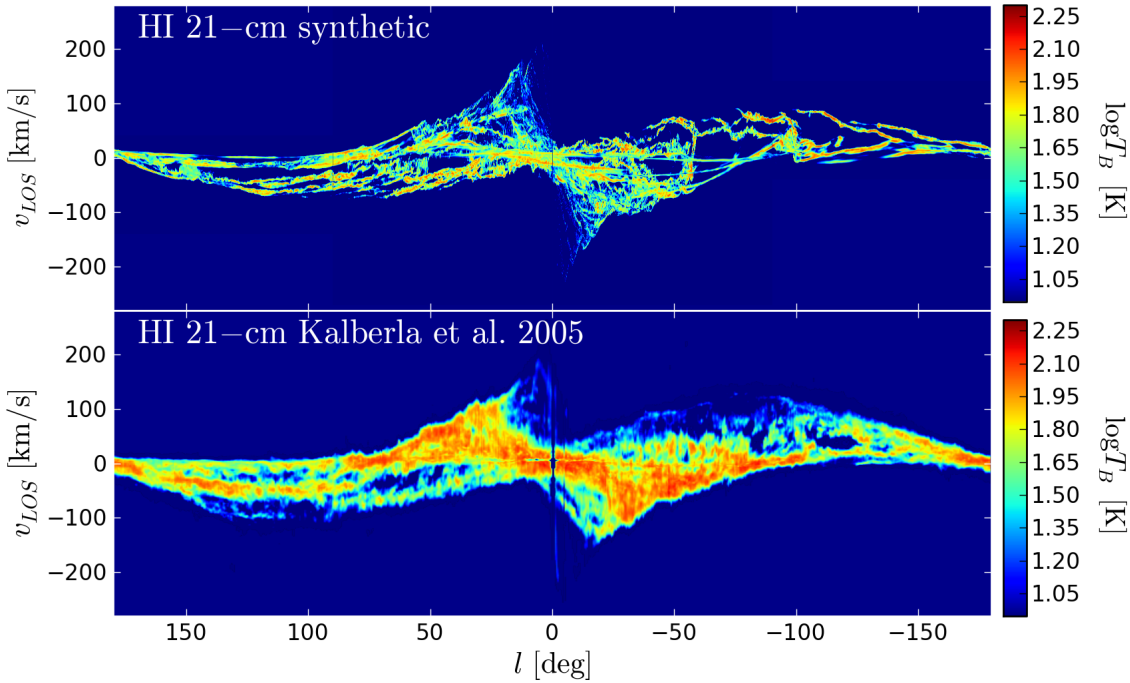


Figure 5.28: Emission map of the HI 21-cm transition created using TORUS. The input model is the 207Myr Bc model, the same as the second map in Figure 5.29. Observational data from Kalberla et al. (2005) is shown for comparison.

compared to observations as we omitted the turbulent broadening present in CO. Arm features can be clearly seen in the second quadrant, even without the broadening to smooth features. The Perseus, Local and Outer arms all appear in the synthetic map. The inner disc at the location of the CMZ shows no emission feature, similar to observations, indicating that in our simulations CMZ hosts just molecular material and a only minor traces of atomic gas.

## 5.7 Discussion

Through the work presented in this chapter we have shown that it is possible to produce many of the observed features of the Galactic CO emission using a system of  $N$ -body particles to represent the stellar distribution. As in Chapter 4, we will use our four best-fitting maps as a basis for our discussion. In Figure 5.29 we show four maps, from top to bottom: Bb, Bc(207Myrs), Bc(292Myrs) and Bd, organised by disc mass. In the left column we show the top-down gas distribution, and in the right the TORUS CO  $l$ - $v$  emission maps, created at the best fitting values of  $l_{\text{obs}}$ ,  $V_{\text{obs}}$  and  $R_{\text{obs}}$ . In each frame we also label significant arm features, with the same nomenclature as used for the Milky Way.

In the heavy disc (Bb, top panel) model the inner  $l$ - $v$  features are similarly inclined to those seen in the observations, namely the Inner Ridge is present, though it is not as clearly defined. The top-down map shows this is a combination of a far and near arm feature. The near arm (labelled Carina) appears weaker than the far inner arm (labelled SCC) and so emission from the far arm can pass through the near arm. This allows for the reproduction in the Carina Arm, which requires an

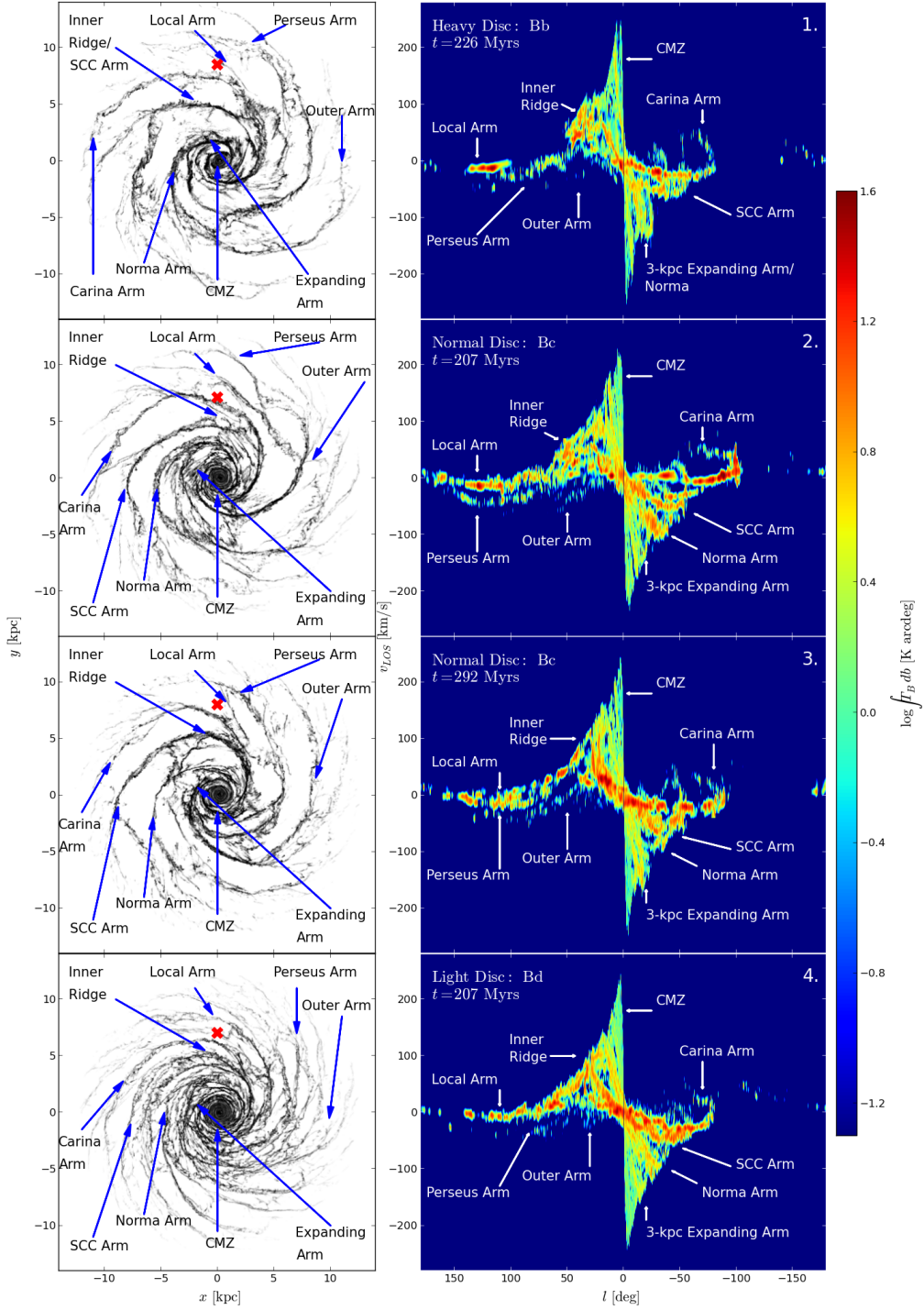


Figure 5.29: Our four best-fitting CO radiative transfer  $l$ - $v$  maps from Fig. 5.27 with their  $x$ - $y$  counterparts. The top-down maps only show gas material that is seen in CO  $l$ - $v$  space; that of the highest density. The cross indicates the observers position (which differs between models). SCC refers to the Scutum-Centaurus-Crux arm in the 4-armed paradigm of the Milky Way, also referred to in the main text as the Inner Ridge when viewed in  $l$ - $v$  space. Arrows indicate locations of prominent features in  $l$ - $v$  space.

arm to be very close to the observers location, while avoiding large amounts of emission at local velocities in the range  $|l| < 50^\circ$ . This was a persistent problem in the maps created from synthetic potentials. The uniform and unbroken nature of the arms made producing the Carina Arm and Inner Ridge impossible. This model also has a looped arm features at very low velocities similar to the 3kpc-Expanding Arm, though is angled steeper in  $l$ - $v$  space than observations. A Local Arm feature has been produced by a spur of the Carina Arm, lying very close to the red-cross in the top-down map. This has been suggested by other studies; that the Local Arm is in fact some spur or inter-arm structure, rather than a primary arm (though the picture is still not clear; Reid et al. 2009, Xu et al. 2013). The caveat of this model is the outer arm structure. Both the Perseus and Outer arms, while clear in the top-down map, are weak or incorrectly placed in  $l$ - $v$  space. The Perseus arm appears at velocities too similar to the local values, making it nearly indistinguishable from the Local Arm in CO emission. The Outer Arm can barely be seen in emission, its presence only given away by a couple of dense pockets of gas.

The second model (Bc) has a slightly lighter disc, and appears a much better fit for many of the  $l$ - $v$  features. The arms in the second and third quadrant are an especially good reproduction of observations. In Figure 5.30 we show a zoom in of this region shown alongside the observational data. The Local, Perseus and Outer arm features are all reproduced and have comparable line-of-sight velocities. The emission is however still somewhat higher than that observed, a problem with all maps produced in this thesis. The top-down map shows the Local and Perseus arms are a bifurcation of the same arm. The Carina hook structure is reproduced, but is present at too great a longitude compared to the observations. This feature can be made to better match, by increasing  $R_{\text{obs}}$ , but at the expense of the other arm features. The Inner Ridge of this model is somewhat poorer than the other models. There is even a void of emission at approximately  $l = 20^\circ$   $v_{\text{los}} = 80 \text{ km s}^{-1}$  where clear emission is seen in observations. The incorrect reproduction of the Inner Ridge is due to the SCC Arm tracing a near-circular arc in the inner disc, which is seen as the steep straight line in the  $l$ - $v$  map. In the other models the SCC arm clearly ‘winds’, i.e. has a non-circular shape, so is seen to be angled in  $l$ - $v$  space.

The second Bc model, created at approximately 100Myrs after the first, appears to be the best reproduction by-eye (the fit-statistic favours the lightest model however). The model shows the Carina, Perseus, Outer and Local Arms as well as an Inner Ridge that is aligned similarly to observations. Local material is again formed by a spur off the Perseus Arm. The Perseus Arm itself is hard to differentiate from the Local and Outer Arm features, which is the main problem with the model. All arm structures in the second quadrant appear at too shallow velocities, implying  $V_{\text{obs}}$  is incorrect or that the model rotation curve is too shallow near the Solar Radius. This model offers the best reproduction of the Inner Ridge and Carina arm simultaneously. The Carina Arm appears to branch away from the SCC Arm (the source of the Inner Ridge) allowing it to be correctly placed in  $l$ - $v$  space without it causing spurious emission in the inner disc, a problem the symmetric fixed potential models persistently encountered. There also appears to be a 4-armed outer structure, with a very strong 2- armed inner structure, which adds weight to the models arms including a strong stellar 2-armed component and weaker 4-armed one in the gas/dust and young stars (Drimmel 2000; Churchwell et al. 2009).

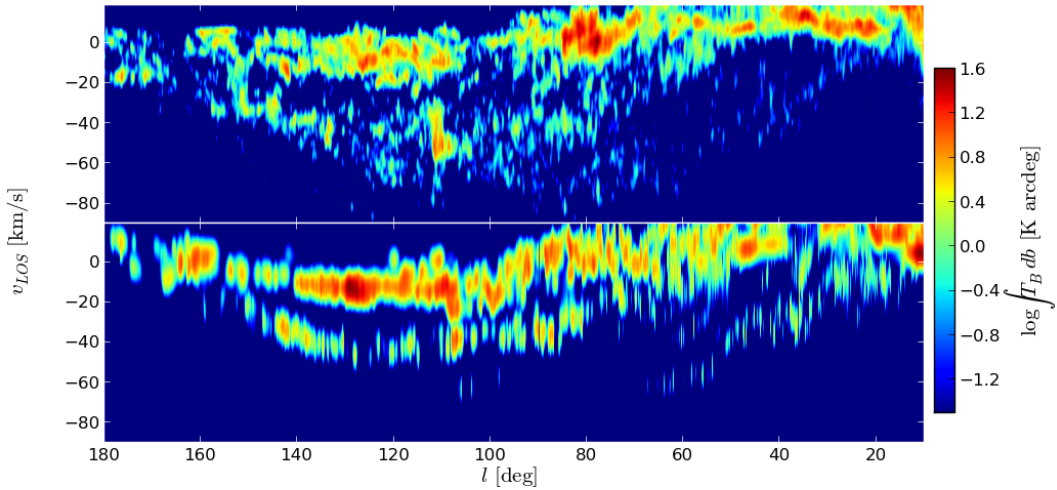


Figure 5.30: Zoom in of the first and second quadrant arm features in CO from the 207Myr Bc arm model (second row, Fig.5.29). Observational data is shown in the upper panel for comparison, the emission strength of which has been increased slightly to be on the same scale as the synthetic map.

Our final model has the lightest disc, and the lowest fit statistic. As with the previous model, there is a good reproduction of the Inner Ridge, Carina Arm and Local material. The Perseus and Outer Arms appear too weak, and there is a significant amount of emission in the inner disc ( $|l| < 30^\circ$ ). While common to all models, this excess emission is especially evident here due to the general flocculent nature of the spiral arms. There is no clear inner disc structure and the many smaller arm features in the inner disc are seen in molecular emission, appearing as a great swath rather than distinct arm features. The flocculent nature is also to blame for the weakness of the Perseus and Outer Arms beyond the Solar radius. It is somewhat alarming that the emission features can be well reproduced by a model with seemingly no clear dominant spiral mode (Fourier analysis indicates  $m \approx 5$ ). While the fit statistic indicates this model is a good fit, it is likely because there is little emission seen in the incorrect place. Coupled with the correct reproduction of the Inner Ridge, Carina and Local Arms, this explains the goodness of the fit. The arm features however seem too weak in the outer disc for this model to be a correct reproduction of our Galaxy. Arms are barely visible in the outer disc, be it in CO or general gas density, meaning they would also not be visible in atomic emission which is simply not the case in observations (see the lower panel of Fig. 5.28).

Overall, the fit statistic favours the light disc model, Bd. However, the features appear too flocculent in the outer disc, and so we favour the second best fit model, Bc. The Bd model provides an excellent fit to the strongest emission regions, that of the Inner Ridge, while the Bc reproduces all other arm features. As the latter arms are weaker in emission in comparison, the fit statistic is lower for the model that fit the Inner Ridge but not the arms, Bd.

### 5.7.1 Comparison to calculations with fixed stellar potentials

It appears that using a live-stellar distribution does a better job than the fixed analytic potentials in many regards. The irregular arm structures created by the live stellar system are able to match emission features simultaneously, such as the Carina arm and Inner Ridge, while symmetric logarithmic spiral arms could not. For example, in the previous Chapters the second quadrant could be fit by moderate to large pitch angles, whereas a much smaller value was needed to fit the Carina feature. The arm numbers of the best fitting models are similar to those suggested by the previous chapters, favouring a 4-armed gas structure to best match the observations. The pitch angles are somewhat higher than inferred previously ( $18^\circ < \alpha < 25^\circ$ ), which are higher than the standard Milky Way models (Vallée 2005). High pitch angles are not uncommon in  $N$ -body simulations (Wada et al. 2011a; Grand et al. 2013) whereas low values are seemingly hard to create without the arms dissipating. Pattern speeds appear to be a function of radius in nearly all cases, with mean values for arms ranging from  $25\text{km s}^{-1}\text{kpc}^{-1} < \Omega_p < 35\text{km s}^{-1}\text{kpc}^{-1}$ , also similar to values found in other studies (Grand et al. 2012; Baba et al. 2013) but higher than those found in the previous chapters. The arms appear material, unlike the steady density waves implied by theories, and material tends to reside in the arms until they shear apart. It may be the case that the Galaxy has no fixed pattern speed, and its spiral arms are also material in nature. It is not unheard of for other galaxies to have pattern speed that decrease with increasing radius (Meidt et al. 2008; Speights & Westpfahl 2012). Bar features that were produced displayed pattern speeds of  $30\text{km s}^{-1}\text{kpc}^{-1}$  (for the disc only, thin bars) and  $45\text{km s}^{-1}\text{kpc}^{-1}$  (peanut/boxy bars).

The total strength of CO emission is more in line with that seen in observations (i.e. weaker) than the previous models, which tended to create extremely bright arm emission structures. The increase in inter-arm features also makes lower strength features corresponding to moderate density material more common. The fit statistic for the emission maps of models is calculated in exact same way as in Chapter 4 and the best-fitting models here provide a systematically better fit than those with fixed potentials (best fitting values give  $\approx 1.05$  for potentials and  $\approx 0.95$  for live discs).

There are some drawbacks to this method however. Each model has far too much emission in the inner disc. This is due to all models here having an inner bulge, which creates high density gas flow around the centre. The initial gas profile, that increases towards the centre, may also be a flaw in the models. The fixed potential calculations effectively had a hole in the inner disc, which resulted in a large dearth of emission at high velocities inside of  $|l| < 20^\circ$ . High gas density was still seen in the inner disc however, but was solely aligned on the  $x_2$  orbits of the bar. As such we believe either an inner bar structure is needed to sweep up molecular material in the inner disc, or that gas density is greatly reduced by some other mechanism. Bars were reproduced however, both in cases with and without an inner bulge. The bulge-free models displayed tentatively good features in the CMZ, but unfortunately were computationally difficult and produced weak outer arm features. The other family of bars reproduced the weak boxy/peanut nature of the Milky Way's bar, but had similar problems as the analytic bars of the previous section (tightly wound arms and very strong nuclear rings at the ILR).

## 5.8 Chapter summary

In this chapter we have shown simulations of the stellar and gaseous components of the Milky Way, rather than using a set of fixed analytic potentials to represent the stars as in Chapters 3 and 4. Various arm and bar morphologies were formed in the stars, with arms appearing transient and material in nature rather than as density waves. The arm number is seen to increase as the disc to halo mass ratio decreases, with arm numbers found to range from  $2 \leq N \leq 5$ . We perform fits to logarithmic spiral features, finding pitch angles in of  $18^\circ < \alpha < 25^\circ$  and pattern speeds in the range of  $20\text{km s}^{-1}\text{kpc}^{-1} < \Omega_p < 38\text{km s}^{-1}\text{kpc}^{-1}$  which decreases with radius rather than maintaining a constant value. Both pattern speed and pitch angle are within the range of values inferred from observations, though in the higher range.

Using the molecular gas in these simulations we then created synthetic  $l$ - $v$  emission maps. A simple method is used to find a best-fitting time-frame and observers coordinates, which are used to reject some outlying models and provide input parameters for the full radiative transfer maps. We find moderate mass discs with a live bulge-disc component provide a good match to the observations, with 4-armed spiral patterns that reproduce many of the arm features. These arms provide a better fit than those using fixed potentials (Chapter 4) and provide a lower fit statistic. The arm features of the Milky Way are thus found to be best-fit by a dynamic and transient disc, displaying a 4-armed pattern in the gas with a pitch angle of approximately  $20^\circ$ .

Some models also formed inner bars, though not in the case of our best fitting models due to the strong inner bulge. We believe a bar is necessary to amend the main flaw in these models; the excess emission at the Galactic centre. It may be that a calculation with a smaller bulge is needed to allow for a bar to form while keeping a distinct outer arm structure.